



Mario Bischof

# **Rebuilding Ekho to profile energy harvester**

## **Bachelor's Thesis**

to achieve the university degree of  
Bachelor of Science

Bachelor's degree programme: Information and Computer Engineering

submitted to

**Graz University of Technology**

Supervisor  
Dipl.-Ing. Hannah Brunner

Evaluator  
Assoc. Prof. Dott. Dott. mag. Dr.techn. Carlo Alberto Boano

Institute of Technical Informatics  
Head: Univ.-Prof. Dipl-Inform. Dr.sc.ETH Kay Uwe Römer

Graz, February 2022



# **Affidavit**

I declare that I have authored this thesis independently, that I have not used other than the declared sources/resources, and that I have explicitly indicated all material which has been quoted either literally or by content from the sources used. The text document uploaded to TUGRAZonline is identical to the present master's thesis.

---

Date

---

Signature



# Abstract

In the context of this Thesis, the usage of energy harvesters like solar panels or thermoelectric elements to power small mobile devices is examined. The combination of transient computing and energy harvesting requires detailed profiles of the used harvesters to enable repeatable testing, debugging and verification. To profile various energy harvesters in different environments, two revisions of the Ekho recorder have been rebuilt. Capable of emulating different load resistances, the Ekho recorders can capture the I-V characteristics of energy harvesters in different operating points. To organize and analyze the recorded data, a database and a toolkit have been implemented. The toolkit provides various means to visualize the recorded data. Additionally, a simple charging circuit can be simulated, making it possible to estimate which type of load can be powered in which harvesting environments. That includes the simulation of two different profiles of transient load behavior (i.e., 'greedy' and 'periodic'). It is shown that under certain conditions, the energy harvested by small solar panels and even thermoelectric elements is sufficient to power low-power wireless sensor nodes that utilize concepts of transient computing.



# Contents

|          |   |           |
|----------|---|-----------|
| <b>1</b> | <b>Introduction</b>                               | <b>1</b>  |
| 1.1      | Problem Statement . . . . .                       | 1         |
| 1.2      | Objective . . . . .                               | 2         |
| 1.3      | Outline . . . . .                                 | 3         |
| <b>2</b> | <b>Background and Related Work</b>                | <b>4</b>  |
| 2.1      | A Typical Energy Harvesting System . . . . .      | 4         |
| 2.1.1    | Energy Harvesters . . . . .                       | 5         |
| 2.1.2    | Energy Storage . . . . .                          | 9         |
| 2.1.3    | Load . . . . .                                    | 10        |
| 2.2      | Transient Computing . . . . .                     | 12        |
| 2.3      | Application examples and prototypes . . . . .     | 13        |
| <b>3</b> | <b>Rebuilding Ekho</b>                            | <b>15</b> |
| 3.1      | Revision A . . . . .                              | 15        |
| 3.1.1    | Hardware . . . . .                                | 16        |
| 3.1.2    | Firmware . . . . .                                | 20        |
| 3.1.3    | Problems . . . . .                                | 22        |
| 3.2      | Revision B . . . . .                              | 23        |
| 3.2.1    | Hardware . . . . .                                | 23        |
| 3.2.2    | Firmware . . . . .                                | 26        |
| <b>4</b> | <b>Toolkit</b>                                    | <b>27</b> |
| 4.1      | SQLite Database . . . . .                         | 27        |
| 4.2      | Surface profiler . . . . .                        | 28        |
| 4.2.1    | 2D I-V curve plots . . . . .                      | 29        |
| 4.2.2    | 3D I-V surface plots . . . . .                    | 29        |
| 4.2.3    | Maximum power point trace . . . . .               | 30        |
| 4.2.4    | Capacitor-charge model . . . . .                  | 31        |
| <b>5</b> | <b>Profiling Energy Harvesters</b>                | <b>34</b> |
| 5.1      | Harvested energy per harvester . . . . .          | 34        |
| 5.1.1    | Solar Panels . . . . .                            | 34        |
| 5.1.2    | Impact of Shadowing, Weather and Season . . . . . | 35        |
| 5.1.3    | Impact of the used solar panel . . . . .          | 37        |
| 5.1.4    | Thermoelectric Elements . . . . .                 | 38        |
| 5.2      | Greedy vs. periodic load behaviour . . . . .      | 39        |

## Contents

---

|   |           |
|---|-----------|
| 5.3 Energy Harvesters as power supply . . . . . | 40        |
| <b>6 Evaluation</b>                             | <b>43</b> |
| <b>7 Limitations</b>                            | <b>46</b> |
| <b>8 Future Work</b>                            | <b>47</b> |
| <b>9 Conclusion</b>                             | <b>48</b> |
| <b>Bibliography</b>                             | <b>50</b> |

# List of Figures

|     |  |    |
|-----|--|----|
| 2.2 | Solar cell equivalent circuit . . . . .                    | 7  |
| 2.4 | Equivalent circuit of a thermoelectric generator . . . . . | 9  |
| 2.6 | A basic harvesting circuit . . . . .                       | 10 |



# List of Tables

|     |  |    |
|-----|--|----|
| 2.1 | Comparison of various energy harvesting technologies . . . . .                     | 6  |
| 2.2 | <i>MSP430F2274</i> current consumption operated with 3.0V supply voltage . . . . . | 11 |
| 3.1 | TMUX1104 Truth Table, take from (“Datasheet TMUX1104,” 2020) . . . . .             | 24 |
| 5.1 | PowerFilm SP3-37: theoretical and measured electrical specifications . . . . .     | 34 |
| 5.2 | Panasonic AM-5610: theoretical and measured electrical specifications . . . . .    | 35 |
| 5.3 | Impact of the used solar panel . . . . .   | 38 |
| 5.4 | Wakefield-Vette TEC-40-39-127: list of experiments . . . . .                       | 39 |
| 5.5 | Harvested energy depending on load behaviour . . . . .                             | 40 |
| 5.6 | Daily energy consumption for different duty cycles . . . . .                       | 41 |
| 5.7 | Simulated on-time in periodic and greedy mode . . . . .                            | 42 |
| 6.1 | Teensy 3.6 ADC: conversion error . . . . .   | 44 |
| 6.2 | Total measurement error Ekho RevA . . . . .  | 44 |
| 6.3 | Total measurement error Ekho RevB . . . . .  | 45 |

# 1 Introduction

Mobile devices within the Internet of Things (IoT) such as wireless sensor nodes often consist of a microcontroller, one or multiple sensors, a wireless transceiver, and an energy source. The microcontroller gathers and processes data from the sensors and uses a wireless transceiver to transfer the collected datasets obtained by the sensors to some sort of base station or another IoT device (Jushi et al., 2016). Wireless sensor nodes are often distributed in an environment that does not allow an external power supply, and are thus commonly powered by batteries. However, using batteries to power devices embedded in wireless sensor networks has some drawbacks, including limited lifetime, battery replacement costs, and an increased form factor (Panahi et al., 2018).

Introducing energy harvesting appears to be one promising solution to overcome these problems. Small sensor nodes can be equipped with an energy harvester (e.g., a solar panel or a thermoelectric generator) to gather freely available energy from the environment, which can be buffered in a small capacitor to power the sensor devices.

Energy harvesting allows the deployment of sensing devices in remote and challenging environments for long periods with little or no need for maintenance (Hester et al., 2014).

## 1.1 Problem Statement

Using ambient energy to power wireless autonomous devices raises new challenges in the hardware and software design of mobile systems. The amount of energy that can be harvested is typically rather low, varying, and unpredictable. Commonly used energy harvesters, such as solar panels or thermoelectric generators, are strongly influenced by the environment in which they operate. A single rising shadow can cut the amount of energy harvested by a solar panel by half within a very short period of time.

Compared to batteries, the amount of energy that can be stored in a tiny capacitor is very limited. Therefore, changes in the environment, like a decrease in light intensity, almost immediately affect the operation of the mobile device at runtime and can cause power failures.

In order to deal with varying and unpredictable harvesting conditions, wire-

less sensor nodes and other mobile devices use a novel approach called transient computing. This approach involves making checkpoints at power failures from which the device can restore the execution state at a later point, once the amount of energy is sufficient to continue its operation (Merrett, 2016).

However, this novel approach is quite challenging to implement and even more challenging to debug and verify. While efficient debugging and verification are crucial for further developments in transient computing, varying and unpredictable environmental conditions make repeatable experiments almost impossible when using traditional methods.

An additional challenge to the rapidly changing harvesting environment is that the amount of harvested energy also depends on the runtime behavior of the powered device. The current delivered by an energy harvester depends on the voltage at which it operates. So-called I-V curves describe this behavior. I-V curves are typically non-linear and feature a maximum power point relating to the optimal operating voltage where the delivered power is at a maximum. In converter-less architectures, the operating voltage of the sensor node equals the operating voltage of the energy harvester. Hence, the sensor nodes operating voltage directly influences the amount of energy that is harvested.

To make experiments with different hardware and software under different environmental conditions repeatable, researchers from Clemson University developed a novel device named Ekho. The device is capable of recording the I-V characteristics of different energy harvesters under transient environmental conditions. That enables repeatable testing of mobile sensing devices, including changing hardware components and running different software while reproducing the same recorded energy harvesting conditions (Hester et al., 2014)

## 1.2 Objective

The goal of this thesis is to provide a database of energy harvesting conditions of different harvesting devices (e.g., solar panels and thermoelectric generators) and to make them available for researches and simulations in the field of transient computing.

Towards this goal, two different versions of the Ekho recorder are rebuilt and tested, and their measurement accuracy is evaluated.

Furthermore, a software tool is implemented that provides means to store, organize, and analyze I-V surfaces recorded by Ekho and allows to visualize the recorded data.

In addition, the software tool features a model to provide insights into what

devices the analyzed energy harvester can power.

Finally, the Ekho recorder and the software tool are used to profile two different solar panels and a thermoelectric generator. Therefore, several days of harvesting activity under different harvesting conditions are recorded and made available via a database.

### 1.3 Outline

Chapter 2 goes into the technical background of the core principles of energy harvesting and transient computing and possible applications for energy harvesters in the Internet of Things. Furthermore, different types of energy harvesters are described. Chapter 3 considers the rebuilding process of Ekho and the implementation of the custom firmware. The implementation of the toolkit capable of processing and evaluating I-V surfaces is described in chapter 4. In Chapter 5, Ekho is evaluated regarding measurement inaccuracy. Chapter 6 deals with the application of Ekho and the implemented toolkit by profiling different energy harvesters in various harvesting conditions. Different load specifications and their impact on the amount of harvested energy are assessed. In Chapter 7, the limitations of the developed toolkit and the Ekho recorder are discussed. Finally, in Chapter 8, all the results are summarized and discussed.

## 2 Background and Related Work

In this chapter, the fundamental structure and the components of a typical energy harvesting system are described. Furthermore, problems that result from its characteristics, like frequent power failures, are discussed. In addition, transient computing, a novel solution to cope with power failures, is explained. Finally, an overview of existing energy harvesting devices and their applications is given.

### 2.1 A Typical Energy Harvesting System

The concept of energy harvesting describes the process of converting ambient energy into electrical energy. In this text, we focus on powering small autonomous electronic devices. Large-scale harvesting systems such as power plants will not be discussed. A typical harvesting system is shown in figure 2.1. It consists of an energy harvester, an energy management unit, an energy storage, and a load. The energy harvester outputs electrical energy, which may have different characteristics depending on the type of the harvester and might raise the need for an energy management unit to modify the output signal (*(Energy harvesting for autonomous systems, 2010)*). For example, a piezoelectric vibration-based energy harvester will output an AC voltage with a specific frequency and magnitude. If this harvester is used to power a typical microcontroller with a DC supply voltage of 3V, a rectification circuit and a voltage regulator is required. Systems featuring

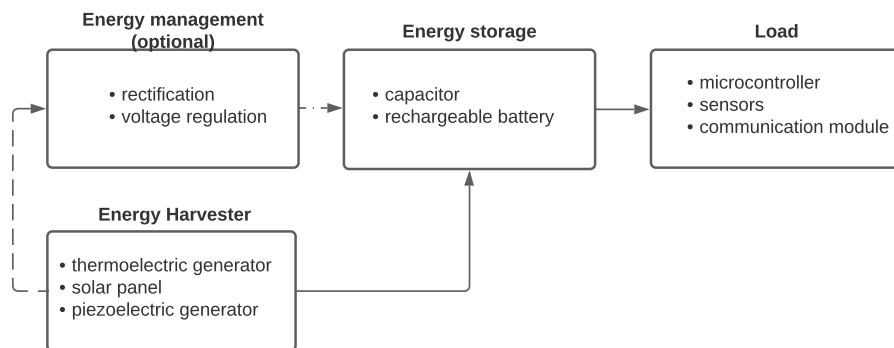


Figure 2.1: Block diagram of an energy harvesting sensor node

an energy management unit are called converter-based. Systems that don't require an energy management unit (i.e., when the output of the harvester matches the required input) are called converter-less (Oh et al., 2017). Since the amount of harvested energy is often inconsistent, means for intermediate energy storage are required. The storage element might be a rechargeable battery or a capacitor. If the capacitor is small, changes in the environment almost immediately affect the operation of the load and can cause power failures. In order to deal with rapidly fluctuating supply voltages, the load device may create checkpoints at power failures. Later on, when there is sufficient energy, the execution state is restored. This novel approach is called transient computing and will be further discussed in section 2.2. A typical load is a wireless sensor node, consisting of a microcontroller, a variety of sensors, and a communication module (*Energy harvesting for autonomous systems*, 2010)). In the following, each part is described in more detail.

### 2.1.1 Energy Harvesters

There are various types of energy sources from which electrical energy can be extracted, but only a few are particularly useful for powering small autonomous devices. The most widely used energy sources are solar- and wind-based, as they are commonly used in large-scale power plants. Solar energy has the highest power density among all ambient energy sources. Solar panels that utilize the photovoltaic effect are available in all sizes and have been used to power small electronic devices for decades. Wind power generators that convert the kinetic energy of air in motion into electrical energy have proven to be applicable for large-scale power plants, but are not yet fully adopted for the use in small-scale systems. Piezoelectric energy harvesters extract electrical energy from mechanical vibrations. They only harvest significant amounts of energy when exposed to high-frequency vibrations as they appear in industrial environments. Furthermore, it is possible to extract electrical energy from radio waves using patch antennas. However, the amount of energy that can be extracted from ambient sources like cellular networks is small and requires large patch antennas. Thermoelectric generators are able to extract electrical energy from temperature differences. The amount of energy that can be harvested is rather low compared to solar energy. Still, the appearance of temperature differences in almost all industrial and natural environments makes an investigation on the applicability as an energy source for autonomous mobile devices interesting. Considering power density as well as the availability in outdoor environments, harvesting systems that use solar and thermal energy sources are further focused in this thesis. Table 2.1 shows the power densities of various harvesting technologies (Cao & Li, 2017).

| Energy source              | Power density          | Harvesting method |
|----------------------------|------------------------|-------------------|
| Solar (outdoor)            | 100 ( $mW/cm^3$ )      | Photovoltaic      |
| Solar (indoor)             | 0,050 ( $\mu W/cm^3$ ) | Photovoltaic      |
| Vibration (human motion)   | 4 ( $\mu W/cm^3$ )     | Piezoelectric     |
| Vibration (machine motion) | 800 ( $\mu W/cm^3$ )   | Electromagnetic   |
| Wind                       | 177 ( $\mu W/cm^2$ )   | Electromagnetic   |
| Thermal (human)            | 60 ( $\mu W/cm^2$ )    | Thermoelectric    |
| Thermal (industry)         | 10 ( $mW/cm^2$ )       | Thermoelectric    |
| Radio frequency (RF-GSM)   | 300 ( $\mu W/m^2$ )    | Patch antenna     |

Table 2.1: Comparison of various energy harvesting technologies

## Solar Panels

Solar panels make use of the photovoltaic effect to convert the energy of the sun into electrical energy. Outdoors, at midday, the power provided by the sun reaches roughly 100 mW/cm<sup>2</sup>. On a cloudy day, the available optical power decreases to approximately 10 mW/cm<sup>2</sup>. However, the light intensity under artificial lighting conditions is much lower. In a typical office room, the available optical power is less than 1mW/cm<sup>2</sup>. Still, those values indicate that solar power could potentially be used to power small electronic devices(Hande et al., 2007).

A part of the available energy can be converted into electrical current and voltage by making use of the photovoltaic effect. When n- and p-type semiconductors are brought together, there's a high concentration of electrons in the n-type area and a high concentration of mobile holes in the p-type area. The difference in concentration leads to electrons migrating from the n-type area to the p-type area while holes are moving from the p-type to the n-type area. These free electrons and holes recombine and leave behind a region of ionized donor impurities in the n-type area and a region of ionized acceptors in the p-type area. On both sides of the junction, regions without free carriers are formed, leading to a voltage difference across the junction. When the p-n junction is exposed to light, photons with more energy than the band-gap energy cause electrons to move from the valence band into the conduction band generating new electron-hole pairs. The electrons again diffuse into the depletion region, where they are affected by the electrical field between the n- and the p-type region. The electrical field pushes them to the opposite side of the p-n-junction, where they recombine and are again separated by the energy of the photons. If a positive voltage that opposes the build-in electrical field (forward bias) is applied to the p-n junction, the field strength is lowered which results in an exponentially increased

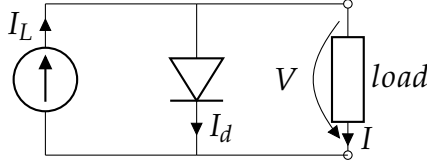


Figure 2.2: Solar cell equivalent circuit

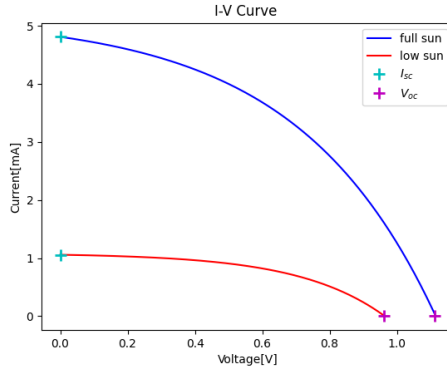


Figure 2.3: I-V curves of a solar cell

diffusion current. If a voltage adding to the build-in field (reverse bias) is applied, the diffusion barrier increases resulting in an exponentially reduced diffusion current. Hence, if an open circuit is considered, a voltage  $V_{oc}$  will be generated. If both sides of the p-n junction are short-circuited, a current  $I_{sc}$  flows.

A simple equivalent circuit modeling an ideal solar cell is shown in figure 2.2. It consists of a current source representing the illumination current  $I_L$  and a parallel diode through which a current  $I_d$  flows. The Shockley diode equation describes the relationship between the current  $I_d$  and the voltage  $V$  across the diode (2.1).

$$I_d = I_0(e^{\frac{qV}{kT}} - 1) \quad (2.1)$$

$I_0$  is the reverse saturation current of the diode,  $T$  is the temperature, and  $k$  represents the Boltzmann constant. According to Kirchhoff's current law, there is a current  $I$  flowing through the load (2.2), causing a voltage drop  $V$ .

$$I = I_d - I_L = I_0(e^{\frac{qV}{kT}} - 1) - I_L \quad (2.2)$$

A solar panel is often characterized using an I-V curve, as shown in figure 2.3).

An I-V curve gives the relationship between the voltage  $V$  and a current  $I$  at the load connected to the solar cell. For each operating voltage  $V$  a certain current  $I$  can be determined. Therefore, an I-V curve holds all information

on the current flow and the harvested power at a given operating voltage. Equation 2.2 shows, that the shape of an I-V curve is characterized by the specifications of the used solar cell, as well as the degree of illumination (Mustansar Hussain, 2018), (*Energy harvesting for autonomous systems*, 2010), (“Alternative energy in power electronics,” 2015).

From the shape of the I-V curve, one can observe that there will be a voltage where the power ( $P = VI$ ) is at a maximum. This point on the I-V curve is called the maximum power point (MPP). In order to harvest the most energy, it is recommended to let the load operate at this point. (Lyden & Ji, 2020).

### Thermoelectric Modules

Thermoelectric modules utilize a temperature gradient to extract electrical energy. They offer two different modes of operation. Firstly they can be used as thermoelectric coolers (TEC) by using the Peltier effect, and secondly, they can be used as thermoelectric generators (TEG) utilizing the Seebeck effect. Both effects describe the interaction and conversion between thermal and electrical energy. It is important to note that products sold as TEG's and products sold as TEC's use the same technical core principles and can both act as thermoelectric coolers and thermoelectric generators. It has even been shown that thermoelectric modules sold as TEC's and used as thermoelectric generators can outperform modules sold as TEG's in specific temperature ranges (Nesarajah & Frey, 2016).

This thesis deals with thermoelectric modules operating in Seebeck (generation) mode only. The Seebeck effect refers to a heat flow caused by a temperature difference that induces a voltage. The generated voltage is proportional to the applied temperature difference ( $\Delta T [K]$ ) and the material-dependent Seebeck coefficient ( $\alpha [V/K]$ ). A typical thermoelectric generator consists of multiple thermoelectric couples connected electrically in series and thermally in parallel. Each couple consists of an n-type and a p-type semiconductor. Applying a temperature gradient causes electrons and holes to diffuse from the hot end to the cold end building up an electrostatic potential.

If an open circuit is considered, the generated voltage  $V_{oc}$  can be calculated by equation (2.3).

$$V_{oc} = N(\alpha_p - \alpha_n)(T_h - T_c) \quad (2.3)$$

$N$  is the number of thermoelectric couples,  $\alpha_p$ , and  $\alpha_n$  are the Seebeck coefficients of the n-type and p-type semiconductor, and  $T_h - T_c$  describes the temperature difference. An equivalent circuit including a load is shown in Figure (2.4).

In that circuit, the thermometric generator is viewed as a thermal battery.  $R_i$  describes the internal resistance of the thermal battery and  $R_L$  the load

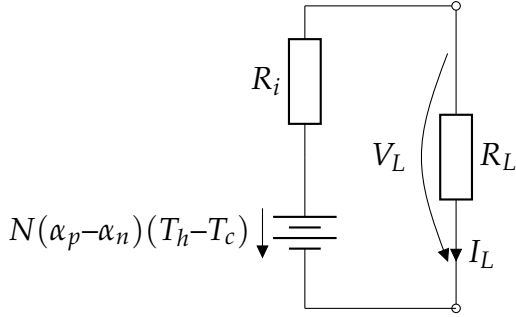


Figure 2.4: Equivalent circuit of a thermoelectric generator

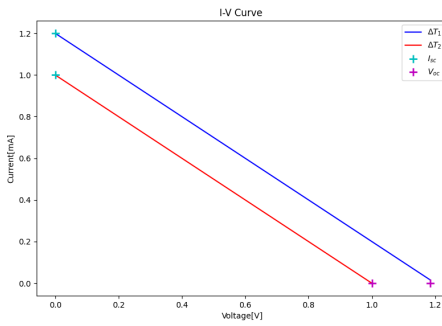


Figure 2.5: I-V curves of a thermoelectric generator

resistance. The voltage drop across the load is given by equation 2.4.

$$V_L = N(\alpha_p - \alpha_n)(T_h - T_c) \frac{R_L}{R_i + R_L} \quad (2.4)$$

Furthermore, equation 2.5 describes the current through the load.

$$I_L = \frac{N(\alpha_p - \alpha_n)(T_h - T_c)}{R_i + R_L} \quad (2.5)$$

Therefore, the voltage and the current through the load depend on the ratio of the internal resistance  $R_i$  and the load resistance  $R_L$  as well as the applied temperature gradient and the characteristics of the used thermoelectric module (Chen, 2019).

Again, an I-V curve is used to visualize the relation between the voltage  $V_L$  and the current  $I_L$ . The I-V curve is obtained by evaluating the equations (2.4) and (2.5) for various values of  $R_L$  and is shown in figure 2.5.

### 2.1.2 Energy Storage

As described in section 2.1.1, the power delivered by an energy harvester is greatly affected by environmental parameters such as light intensity or

temperature differences. In addition, the I-V characteristics of an energy harvester add a dependency on the operating voltage and thus, make the power delivery even more unpredictable and inconsistent. One solution could be to use an adequately large rechargeable battery that can compensate for changes in power delivery and prevent power failures. However, batteries as an energy storage device have multiple shortcomings that relate to physical limitations (size/weight), as well as limited lifetime and safety risks due to their electrochemical properties (Ahmed et al., 2018a). An alternative is the usage of a small capacitor as an energy buffer.

A very basic harvesting circuit is shown in figure 2.6. It consists of an energy harvester (i.e a solar cell), a diode, a capacitor and a load.

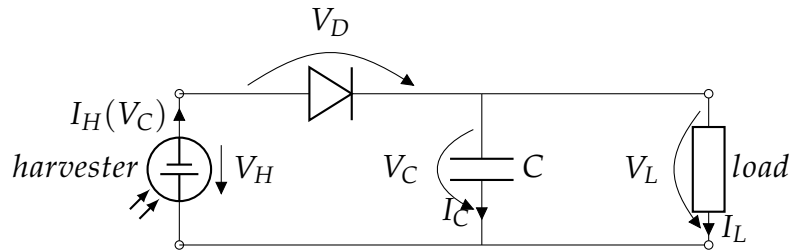


Figure 2.6: A basic harvesting circuit

By applying Kirchhoff's current law, the current  $I_C$  that charges or discharges the capacitor is calculated via  $I_C = I_H - I_L$ . Hence, the capacitor is charging when the current draw of the load is smaller than the current supplied by the harvester and discharging when the load current is bigger than the current provided by the harvester. The resulting capacitor voltage is described by equation 2.6. The current supplied by the harvester decreases proportionally to the operating voltage ( $V_H = V_C - V_D = V_L - V_D$ ). The exact relation is individual for each harvesting environment and is described by an I-V Curve.

$$V_C = \frac{1}{C} \int I_C(t) dt = \frac{1}{C} \int I_H(t) - I_L(t) dt \quad (2.6)$$

### 2.1.3 Load

As described previously, a typical load consists of a microcontroller, sensors and a radio transceiver. Since the amount of energy that can be harvested is limited, only low-power microcontrollers can be used. Microcontrollers in wireless sensor networks usually have very low sleep currents, fast wake-up times, and interfaces to a range of peripherals like sensors or radio transceivers. An example for a low-power microcontroller that is well suited for the use in wireless sensor nodes as well as transient computing is the 16-bit Texas Instruments *MSP430*. In active mode, an *MSP430F2274* typically

consumes  $390\mu A$  operating at  $1MHz$  with a  $3V$  power supply. Furthermore, the *MSP430* features four different low-power modes. In all low-power modes, the CPU is disabled. In the more shallow low-power modes, certain clocks and DC-DC converters are disabled. In LPM<sub>4</sub>, the deepest sleep mode, the system can only be woken up by external interrupts. Microcontrollers in wireless sensor nodes typically spend a high percentage of time in low-power modes to keep power consumption to a minimum. Figure 2.2 shows the current consumption of an *MSP430F2274* microcontroller operating in different modes (“*MSP430F22x2, MSP430F22x4 Mixed Signal Microcontroller datasheet (Rev. G)*,” 2021).

| Mode                                 | Operational restrictions   | Current Consumption ( $\mu A$ ) |
|--------------------------------------|--|---------------------------------|
| Active mode - 1mHz (AM)              | - All clocks active  | 390                             |
| Low-power mode 0 (LPM <sub>0</sub> ) | - CPU disabled<br>- MCLK disabled  | 90                              |
| Low-power mode 1 (LPM <sub>1</sub> ) | - CPU disabled<br>- MCLK disabled<br>- DCO dc-generator disabled<br>(if DCO not used in active mode)                             | unknown                         |
| Low-power mode 2 (LPM <sub>2</sub> ) | - CPU disabled<br>- MCLK and SMCLK disabled<br>- DOC dc-generator remains enabled<br>- ACLK remains active                       | 25                              |
| Low-power mode 3 (LPM <sub>3</sub> ) | - CPU disabled<br>- MCLK and SMCLK disabled<br>- DOC dc-generator disabled<br>- ACLK remains active                              | 0.6 - 0.9                       |
| Low-power mode 4 (LPM <sub>4</sub> ) | - CPU disabled<br>- ACLK disabled<br>- MCLK and SMCLK disabled<br>- DOC dc-generator disabled<br>- Crystal oscillator is stopped | 0.1                             |

Table 2.2: *MSP430F2274* current consumption operated with  $3.0V$  supply voltage

Table 2.2 shows, that the current consumption in active mode is several magnitudes higher than in the low-power-modes. The energy reduction achieved by duty-cycled operations can be calculated by equation 2.7 (*Energy*

*harvesting for autonomous systems, 2010).*

$$EnergyReduction = (1 - DC)(1 - \frac{P_{sleep}}{P_{active}}) \quad (2.7)$$

Furthermore, the transceiver of wireless sensor nodes consumes a significant amount of power when transmitting or receiving. Commonly used IEEE 802.15.4/ZigBee low power transceivers consume between 15 and 60mA at 3V to 5V when sending or receiving. Bluetooth Low Energy (BLE) transceivers have a similar power consumption and are thus also suitable for use in wireless sensor nodes.

The power consumption of the sensing subsystem depends on the used sensor type. For light or temperature sensors, the sensing subsystem will be the wireless sensor node's least power-consuming component. However, for certain types of sensors, like GPS modules, the power consumption is not negligible (Shaikh & Zeadally, 2016).

## 2.2 Transient Computing

When the amount of energy that can be harvested is small, and just a small capacitor is used as an energy storage, power failures will occur frequently. Even designs that feature a super-capacitor or a battery might experience power failures when a discharged state is reached. Therefore multiple novel methods have been developed, which may be summarized under the term "transient computing." All of them address the issue of ideally pausing and restarting computations with respect to the available power. Energy harvesting systems that rely on transient computing share a microcontroller that features non-volatile memory such as FRAM (ferroelectric RAM) or flash memory. Non-volatile memory is used to store and restore an execution state and some data (Ahmed et al., 2016).

One of the first proposed methods in transient computing was the Mementos system, a software-based approach. It is built upon an energy-aware checkpoint system. At compile time, so-called trigger points are inserted into the program via LLVM optimization passes. There are calls to functions in the Mementos library that estimate the available energy by measuring the voltage of the device's energy buffer using the Analog-Digital Converter (ADC) of an MSP430 microcontroller. The voltage measured is then compared with a checkpoint threshold voltage ( $V_{thresh}$ ). The threshold is determined conservatively by assuming that no further energy will be harvested between the trigger point and a power failure. If the measured voltage

is below the threshold, a checkpoint is created by copying relevant program states (i.e. registers, stack, globals,...) to non-volatile memory. Mementos wraps a program's *main()* function with code that searches for an active checkpoint for restoring execution. Upon reboot, after a power failure, the contents of the checkpoint are copied back into RAM. When finally the stack pointer and the program counter are restored, the control is transferred back to the program, and the execution continues from where it has been left over (Ransford et al., 2011).

Software-based approaches like Mementos effectively allow the recovery of a past execution state. However, a certain amount of code size overhead and an execution time overhead caused by periodically inserted trigger-points are inevitable. Furthermore, deciding where to insert trigger points and checkpoints at compile time is not trivial. To overcome these drawbacks, hardware-assisted transient computing has been proposed (Ahmed et al., 2018b).

The Hibernus approach was one of the first hardware-assisted transient computing approaches for energy harvesting systems. Hibernus uses a comparator that triggers a hardware interrupt when the supply voltage drops below a threshold voltage and saves a snapshot of all volatile memory into non-volatile FRAM. When the supply voltage again increases and surpasses the threshold voltage, another hardware interrupt restores the snapshot (Balsamo et al., 2015).

### 2.3 Application examples and prototypes

Although energy harvesting wireless sensor nodes (EH-WSN) are not yet commercially available, there exist multiple prototypes using different energy sources. Most of them feature rechargeable batteries or supercapacitors as energy buffers. There exist various prototypes utilizing the photovoltaic effect. An example is the ISEH (Intelligent Solar Energy-Harvesting) system proposed in 2015. It consists of a ZigBee transceiver, a rechargeable lithium battery, an ARM Cortex-M0-based microcontroller and a solar panel that can deliver up to 450mW at 5V. With multiple sensors (dissolved oxygen, PH, temperature...) attached, the ISEH prototype reaches a peak power consumption of 460mW at 5V. Though, this EH-WSN is not known to be tested in field for a specific application. (Li & Shi, 2015)

Prototypes with thermoelectric harvesting systems power wireless sensor nodes have been designed too. However, the amount of harvested energy is much lower. A thermoelectric EH-WSN that uses just a capacitor as an energy buffer was proposed in (Im et al., 2020). The module consists of

## 2 Background and Related Work

---

a microcontroller (atmega16L), a Bluetooth module (BoT-CLE100), and a temperature and humidity sensor (HT01DL). A custom energy management integrated circuit (EMIC) is used for maximum power point tracking (MPPT) and voltage regulation. The node has been successfully tested for a temperature difference of 70°C between the thermoelectric generator's hot and cold sides. It has been proposed that this EH-WSN could be used in various environmental monitoring applications. However, this prototype was never tested in an open field trial.

Another thermoelectric EH-WSN that was actually deployed and tested in field was presented in (Ikeda et al., 2020). The prototype is designed for monitoring soil humidity and temperature. A thermoelectric harvester gathers energy utilizing temperature gradients between near-surface air and shallow underground soil. Experiments show that  $100\mu W - 370\mu W$  can be harvested, which is sufficient to power a wireless microcontroller that performs soil monitoring.

# 3 Rebuilding Ekho

Designing wireless sensor nodes and other mobile devices that are solely powered by ambient energy sources raises a lot of challenges. If energy harvesting concepts are combined with methods in transient computing, design complexity increases even further. One key issue is making debugging and verification repeatable and reproducible. Since environmental conditions like light intensity or temperature gradients are varying and unpredictable, repeating the same experiment may lead to different results. Additionally, changes in hardware or software will lead to different behavior. That applies, even if the harvesting conditions remain constant since the amount of harvested energy also depends on the operating voltage of the tested device. When harvesting circuits with tiny capacitors as energy buffers like the one described in 2.1.2 are used, the operating voltage directly corresponds to the capacitors' state of charge. The state of charge is determined by the current drain of the test device, as well as the supply current. Hence, even the runtime behavior of the test device alters the amount of energy harvested and the rate of power failures. As described in 2.1.1, dependencies on the operating voltage can be depicted in I-V curves. An I-V curve holds information on the amount of current delivered, at any given operating voltage, for a fixed point in time.

The Ekho recorder is capable of continuously recording I-V curves and consequently generating a dataset that contains multiple I-V curves together with a timestamp. By adding a time axis, multiple I-V curves form a so-called I-V surface. This dataset holds all information to capture transient environmental conditions. The recorded data can later be used to simulate the same harvesting environment over and over again and thus makes experiments repeatable and reproducible. For this thesis, two different revisions of the Ekho recorder were rebuilt and tested.

## 3.1 Revision A

The Ekho recorder consists of a Teensy 3.6 development board which is connected to an analog frontend. The Teensy 3.6 controls a digital potentiometer located on the frontend board via an I<sup>2</sup>C interface. By sweeping the load resistance, different current draws can be simulated. Hence, the variable load makes it possible to emulate various operating points to cover

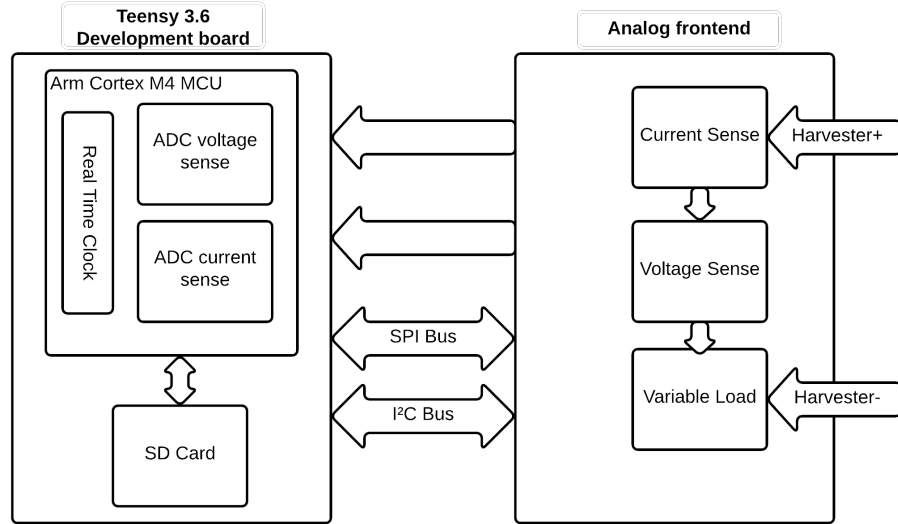


Figure 3.1: Ekho RevA Block diagram

different parts of I-V curves. Every time the load resistance changes, voltage, and current measurements are performed. The measured voltages are then converted to digital values by the Teensy's internal ADC. A timestamp is added, and after some reprocessing, the recorded I-V pairs are written to an SD Card. Figure 3.1 shows a simplified block diagram of the Teensy 3.6 development board connected to the analog frontend.

### 3.1.1 Hardware

#### Teensy 3.6 development board

The Teensy 3.6 is a development board based on a 180MHz NXP MK66FX1MoVMD18 32-bit ARM Cortex M4F microcontroller. The microcontroller features 1.25MB of flash memory, 256KB of RAM, and 4KB of EEPROM, which is absolutely sufficient for common sensing applications. Furthermore, the K66 family features two onboard 16-Bit SAR (Successive-approximation) ADCs. Ekho uses them for converting analog signals obtained from current and voltage measurement to digital values. The conversion rate of the two ADCs is specified with 37 to 461kS/s, building a theoretical maximum measurement frequency. Another crucial onboard component for this project is the real-time clock. It is used to generate accurate timestamps that are bound to every recorded I-V pair. A separate 32.768kHz crystal is used to generate the real-time clock. If a 3V coin cell is connected to the VBAT and GND pins, timekeeping is maintained, even when the main power is off. Furthermore, the microcontroller contains a Secure Digital Host Controller (SDHC) that is



Figure 3.2: Teensy 3.6 development board

used to manage SD-Cards via SDIO interface (“Kinetis K66 Sub-Family,” 2017). Conveniently, the Teensy 3.6 development board offers an integrated Micro SDHC slot. In total, 64 input/output signal pins are accessible on the Teensy 3.6 development board. Twenty-five of these pins can be used for reading analog inputs. Two of them are used for current and voltage measurements in this project. For communicating with external chips, three SPI ports (signals MOSI, MISO, SCK) are provided. In this project, the SPI interface is used to drive Programmable Gain Amplifiers (PGA) on the analog frontend. In addition, the Teensy’s MCU provides four ports for I<sup>2</sup>C communication. However, Ekho uses just one I<sup>2</sup>C port for communication with the digital potentiometer. The Teensy 3.6 board may be powered by using a micro USB cable, which is linked to the VUSB and the VIN pins. A voltage regulator reduces the 5V from the USB power supply to 3.3V, which is appropriate to power the MK66FX1MoVMD18 microcontroller (“Teensy® 3.6 Development Board,” 2017). The Teensy 3.6 development board is shown in figure 3.2.

#### Analog frontend

The analog frontend, shown in figure 3.3 has been designed by (Hester et al., 2014), and makes it possible to accurately measure current and voltage provided by arbitrary energy harvesters. The two-layer PCB board can be divided into three functional units: voltage regulation, a SD card slot, and a measurement unit.



Figure 3.3: Ekho RevA analog frontend

### 3 Rebuilding Ekho

---

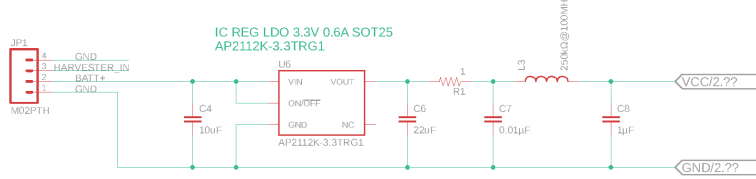


Figure 3.4: Ekho RevA voltage regulation

The voltage regulation unit is based on a low dropout voltage controller (LDO). The AP<sub>2112</sub>K-3.3TRG1 LDO is capable of reducing an input voltage of up to 6V to an output voltage of 3.3V (“AP<sub>2112</sub> Datasheet,” 2017). Figure 3.4 shows the voltage regulation circuit, where the power supply should be connected to *BATT+* and *GND*, while *VCC/2* and *GND/2* are connected to the Teensy’s *VIN* and *GND* pins. Using this voltage regulation circuit, it is possible to power the Teensy 3.6 without using a USB cable (e.g with three serially connected AA-Mignon cells).

The SD Card slot on the analog frontend is connected to the Teensy via an SPI interface. However, the SD Card slot on the PCB is redundant since the Teensy 3.6 features its own SD Card Slot and was therefore never used for this thesis.

The measurement unit consists of a current and voltage sense circuit, as well as a digital potentiometer, as shown in figure 3.5. The harvester under test is attached to the *H+* and *H-* pins of the analog frontend. The current first flows through a shunt resistor ( $R_5 = 10\Omega$ ), which is used for measuring the current delivered by the harvester. Using an SPI programmable gain amplifier differential input (MAX9939), the voltage drop over the shunt resistor is amplified to match the input voltage range of the Teensy’s ADC. The output of the PGA is directly connected to an analog input pin (*CS\_ADC*) of the Teensy 3.6. The amplification factor can be set to gains from 0.2 to 157. In addition to the gain, also the input offset voltage ( $V_{OS}$ ) can be adjusted between  $\pm 17mV$  via the SPI interface. The MAX9939 features three registers: one shift register, and two internal registers. The internal registers are each 8-bit wide and can modify the gain, offset voltage, and the programmable gain amplifier’s operating mode.

$$V_{OUTA} = \frac{V_{CC}}{2} - Gain \cdot (V_{INA} - V_{INB}) + Gain \cdot V_{OS} \quad (3.1)$$

Equation 3.1 shows the relationship between the differential input and the output of the PGA, where  $V_{OUTA}$  is the output voltage,  $V_{CC}$  the supply voltage (i.e. 3.3V), and  $V_{OS}$  the adjustable offset voltage.  $V_{INA}$  and  $V_{INB}$  are the electrical potentials before and after the shunt resistor  $R_5$  (“MAX9939 Datasheet,” 2019).

### 3 Rebuilding Ekho

---

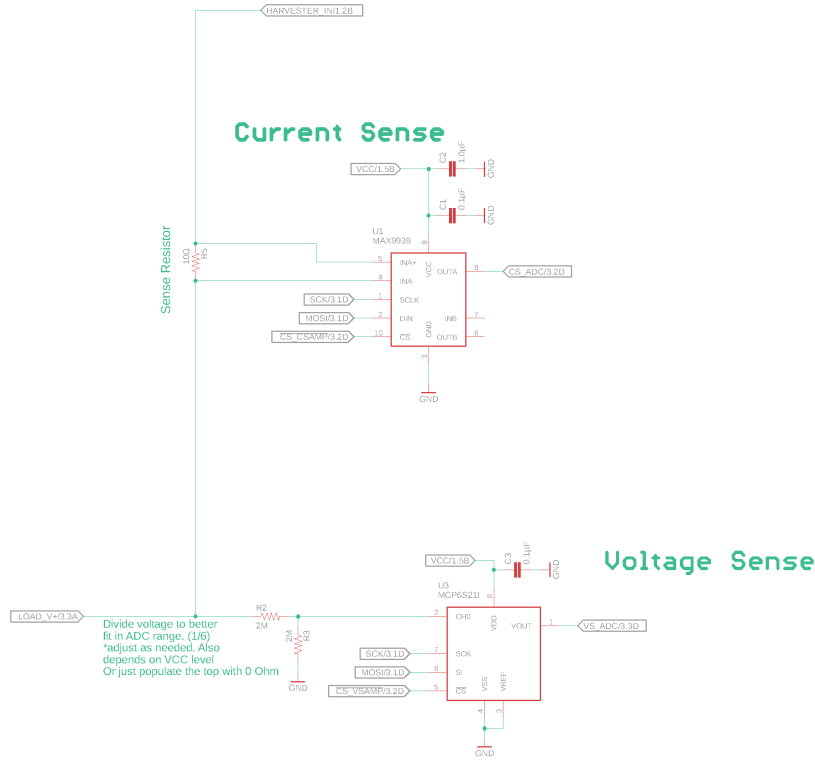


Figure 3.5: Ekho RevA current and voltage sense

A digital potentiometer is connected in series to the shunt resistor together with a parallel voltage divider that adjusts the voltage to better fit in the Teensy's ADC input range. In addition, a MCP6S21I SPI programmable gain amplifier is used as a voltage follower in order not to burden the harvester. Equation 3.2 shows the relationship between the harvesters output voltage and the input voltage of the Teensy's ADC. The whole current and voltage sense circuit is shown in figure 3.5

$$V_{VS\_ADC} = V_{HARVESTER\_IN} \cdot \frac{R_{load} \cdot (R_3 + R_2)}{R_{load} \cdot (R_3 + R_2) + R_5 \cdot (R_{load} + R_3 + R_2)} \cdot \frac{R_3}{R_2 + R_3} \quad (3.2)$$

Since the shunt resistance  $R_5$  is relatively small compared to the load resistance  $R_{load}$ , and the voltage dividing resistors  $R_2$  and  $R_3$  are magnitudes larger than the load resistance, equation 3.2 can be further simplified to 3.3.

$$V_{VS\_ADC} = V_{HARVESTER\_IN} \cdot \frac{R_3}{R_2 + R_3} \quad (3.3)$$

with  $R_5 \ll (R_{load} \parallel (R_2 + R_3))$  and  $R_{load} \ll (R_2 + R_3)$

An AD5242BRUZ100-RL7 digital potentiometer is shown in figure 3.6. It

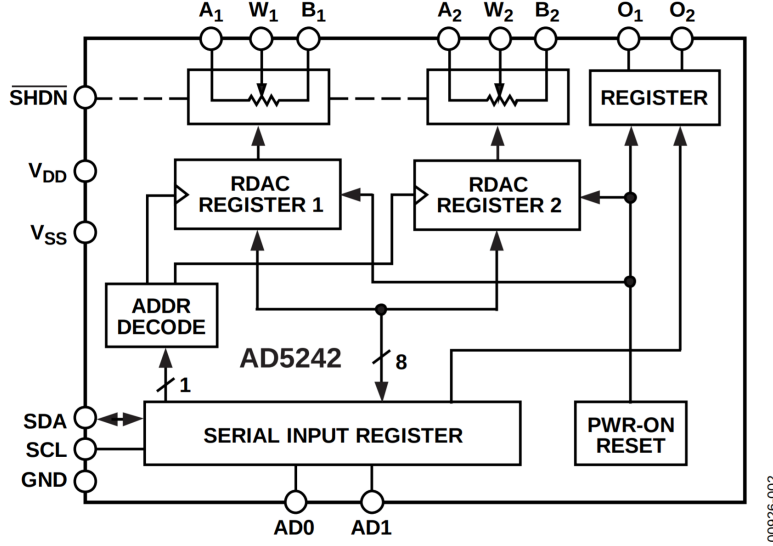


Figure 3.6: AD5242 functional block diagram, taken from (“Datasheet AD5241/AD5242,” 2015).

is used to simulate the load and is connected to the Teensy via an I<sup>2</sup>C Bus to perform a resistance sweep. The AD5242 features two variable resistors. The resistance between each A terminal and wiper (W) and between wiper (W) and B terminal is programmable via setting bits of an 8-bit register. The AD5242 is connected to the measurement circuit with the  $W_1$  and the  $B_2$  terminal in this project. Equation 3.4 gives the relation between the programmed 8-bit code  $D$  and  $R_{WB}$ . The relation between  $R_{WA}$  and  $D$  is given by equation 3.5.  $R_{AB}$  is the nominal resistance from terminal A to terminal B and is 100k for this specific digital potentiometer.  $R_W$  is the wiper resistance and also determines the minimum resistance (60Ω).

$$R_{WB}(D) = \frac{D}{256} \cdot R_{AB} + R_W \quad (3.4)$$

$$R_{WA}(D) = \frac{256 - D}{256} \cdot R_{AB} + R_W \quad (3.5)$$

Hence, for the given wiring, a maximum resistance of 200kΩ can be reached (“Datasheet AD5241/AD5242,” 2015).

### 3.1.2 Firmware

The firmware is based on a version published by Josiah Hester, Timothy Scott, and Jacob Sorber from Clemson University on GitHub (Josiah Hester, 2019). The firmware has been modified and advanced for this thesis. The most significant changes involve adding support for interfacing with a micro

SD card and adding timestamps to the recorded IV-Curves. While the original firmware has been meant to send recorded data directly to a PC via USB for further processing, the firmware has been tuned to allow autonomous long-term recording of harvesting environments without relying on external peripherals. Additionally, changes were made in the configuration of the programmable gain amplifiers used in the analog frontend for better matching the characteristics of the energy harvesters profiled in this thesis. Furthermore, the firmware has been ported from a pure Arduino project to a PlatformIO project to make development independent from the Arduino IDE while keeping the Arduino framework.

## Structure

The program consists of a `setup()` and a `loop()` function. Those functions are called by the `main()` function, which the Arduino core library provides. The `setup()` function is called once the program is started, and the `loop()` function is called in an endless loop afterwards. First, in the `setup()` function, the GPIO's of the peripherals are configured accordingly. Once that is completed, the gains and the offset voltages of the programmable operational amplifiers are configured by SPI transactions. The exact gain and offset configuration needs to be individually adjusted for each tested energy harvester. Furthermore, the Teensy's internal ADCs are configured. Again the configuration depends on the energy harvester that is being tested. The ADCs provide a resolution of up to 16-bit, however for this thesis, we used no more than 12-bit due to noise. If conversion speed is not critical, one can use the averaging conversation feature for a less noisy output. Finally, the SD Card library is initialized, and all old files are removed from the SD Card.

After the setup is completed, I-V measurements are performed and recorded in the `loop()` function. Upon each iteration, the resistance of the programmable potentiometer is changed, and a read from both the current and the voltage sense ADC is performed. Afterwards, the read digital values are converted to voltage and current entities. Equation 3.6 and equation 3.7 describe the relationship between the read ADC values ( $D_{ADC0}, D_{ADC1}$ ) and the current ( $I_{SD}$ ) and voltage ( $V_{SD}$ ) entities written to the SD Card. The first part of equation 3.6 results from the biasing characteristics of the current sense PGA, which was described in equation 3.1.

$$I_{SD}[\text{mA}] = \left( \frac{2^N}{2} - D_{ADC0} \right) \cdot 1000 \cdot \frac{V_{ref}}{2^N} \quad (3.6)$$

$$V_{SD}[\text{V}] = D_{ADC1} \cdot \frac{V_{ref}}{2^N} \quad (3.7)$$

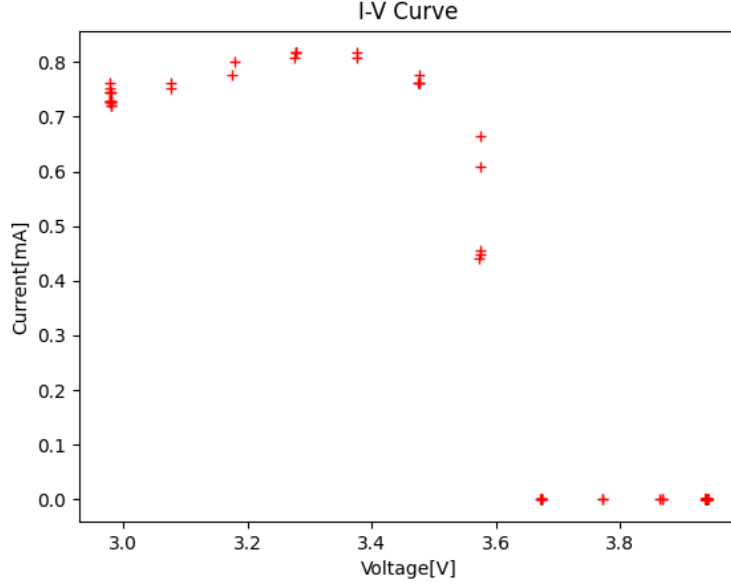


Figure 3.7: Erroneous I-V curve recorded by Ekho for higher input voltages

For each potentiometer loop, a timestamp is computed by using the Teensy's real-time clock. One potentiometer loop represents one IV-Curve, therefore upon each loop, a curve index is increased. After every IV measurement, the timestamp, the curve index, as well as the respective current and voltage entities are written to the internal SD Card.

### 3.1.3 Problems

The first design works well for profiling low voltage harvesting environments. However, some discrepancies between expected and measured current becomes noticeable when using harvesters that output higher voltages. The problem occurs using the following experimental setup: A power supply is used to simulate an energy harvester and is connected to Ekho. The current limit is set to  $0.8mA$ , and the voltage was swepted between  $3V$  and  $4V$ , while the Ekho's potentiometer is set to minimum resistance ( $60\Omega$ ). Figure 3.7 shows the output of the experiment. It can be observed that the measured current starts to break down to almost  $0mA$  once a voltage of  $3.4V$  is exceeded. However, a current flow through  $R_5$  could be confirmed when connecting an ampermeter in series between the power supply and Ekho's *Harvester\_IN* port. Hence, it seems likely that Ekho's current sense unit experiences faulty behavior.

The datasheet of the PGA (MAX9939) used to amplify the voltage drop across  $R_5$ , defines an input common-mode range  $V_{CM}$  between  $-V_{CC}/2$  and  $V_{CC} - 2.2V$ , for which a given Common-Mode Rejection Ratio (CMRR)

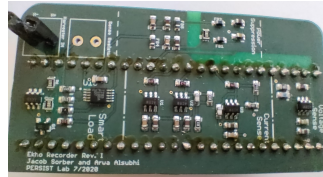


Figure 3.8: Ekho RevB analog frontend

applies. Outside the input common-mode range, behavior is unspecified. Equation 3.8 gives the maximum input voltage  $Harvester\_IN\_max$ , for which the common-mode range is not violated can be calculated. For example, when 4V are applied to the measurement circuit, the common-mode voltage equals 3.43V and is clearly outside the specified common-mode range. That explains the erroneous current measurements.

$$V_{HARVESTER\_IN\_max}[V] = (V_{CC}[V] - 2.2[V])) \cdot \frac{1}{1 - \frac{R_5}{R_5 + \frac{R_{load} \cdot (R_2 + R_3)}{R_{load} + (R_2 + R_3)}}} \quad (3.8)$$

## 3.2 Revision B

The analog frontend of the first Ekho showed issues measuring greater voltages. However, this thesis needs the ability to profile harvesters that output voltages high enough to power MCU's like an MSP430. That's why an advanced version of Ekho was rebuilt. Again the design was provided by Clemson University.

### 3.2.1 Hardware

The advanced version of Ekho uses the same Teensy 3.6 but features a significantly advanced analog frontend.

#### Analog frontend

The analog frontend, shown in figure 3.8 has been designed by Jacob Sorber and Arwa Alsubhi from Clemson University. Unlike the first Ekho, it is built as a single-layer PCB board. The new analog frontend features two functional units: A power ripple suppression and a measurement unit.

The advanced Ekho can only be powered via the Teensy and does not feature a voltage regulation unit like the original model. A power ripple suppression unit is used to remove USB and digital noise as well as switching ripple. Figure 3.9 shows the power ripple suppression unit. This filter

### 3 Rebuilding Ekho

---

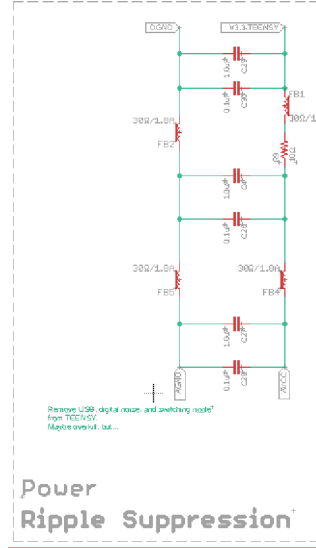


Figure 3.9: Ekho RevB power ripple suppression unit

is connected to the Teensy via the  $V_{3.3}$  and digital ground  $DGND$  port. The connection to the analog frontend is established via the  $AV_{CC}$  and the  $AGND$  ports.

The measurement unit is located between the harvester (port  $HARV+$ ) and the Teensy’s analog ground ( $AGND$ ). It consists of a variable load, a current sense circuit, and a voltage sense circuit. The load is realised via various resistors ( $R_{13} = 41\Omega$ ,  $R_{21} = 1k\Omega$ ,  $R_{26} = 5.1k\Omega$ ,  $R_{27} = 5k\Omega$ ) that can be selected via a Texas Instruments TMUX1104DGSR 4:1 precision multiplexer. The multiplexer features two pins ( $A_0$ ,  $A_1$ ) that control the switches  $S_1$  to  $S_4$ , when the  $EN$  pin is high. The corresponding truth table is shown in 3.1 (“Datasheet TMUX1104,” 2020).

| <b>EN</b> | <b>A1</b> | <b>A0</b> | <b>Selected Input Connected To Drain (D) Pin</b> | <b>Load resistance</b> |
|-----------|-----------|-----------|--|------------------------|
| 0         | $x$       | $x$       | All channels are off                             | $\infty$               |
| 1         | 0         | 0         | $S_1$  | $R_{27} = 100k\Omega$  |
| 1         | 0         | 1         | $S_2$  | $R_{26} = 5.1k\Omega$  |
| 1         | 1         | 0         | $S_3$  | $R_{21} = 1k\Omega$    |
| 1         | 1         | 1         | $S_4$  | $R_{13} = 51\Omega$    |

Table 3.1: TMUX1104 Truth Table, take from (“Datasheet TMUX1104,” 2020)

In addition, an Omnisem BSS138 n-channel enhancement MOSFET is connected in series and can be used for fine-tuning the total load resistance. The gain drain-source resistance  $R_{DS}$  is controlled by the gate-source voltage  $V_{GS}$  which is set using the Teensy’s Digital-Analog-Converter (DAC). Be-

### 3 Rebuilding Ekho

---

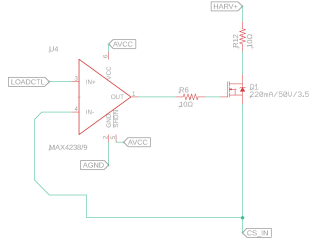


Figure 3.10: Ekho RevB MOSFET load

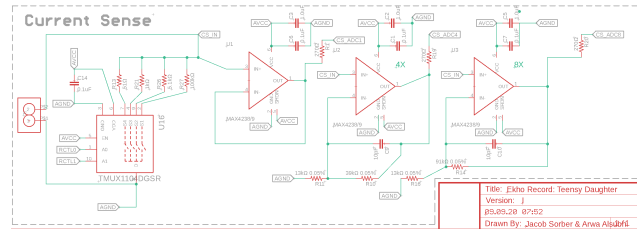


Figure 3.11: Ekho RevB current sense

tween the Teensy's DAC and the MOSFET, a MAX4238 amplifier is used as a voltage follower. The MOSFET based resistance unit is shown in figure 3.10.

For measuring the current supplied by the device under test, the load resistors selected by the multiplexer are used as shunt resistors. The voltage drop at the shunt resistor is then adjusted to the Teensy's ADC input range via three different amplification circuits. Each amplification circuit is built upon a MAX4238 amplifier and wired as a non-inverting amplifier as shown in figure 3.11. The output of each amplifier is connected to a different analog input pin of the Teensy. Hence, it is possible to take three samples, one per amplification circuit. Afterwards the best fitting output is selected, while the others are discarded.

Voltage measurements are performed by a voltage divider and an ad-

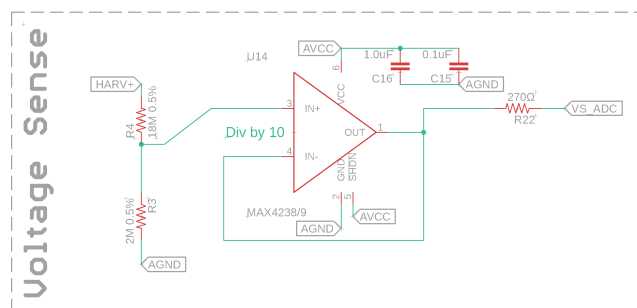


Figure 3.12: Ekho RevB voltage sense

ditional amplifier connected in parallel to the load. The voltage divider shown in figure 3.12, is formed by the resistors  $R_4 = 18M\Omega$  and  $R_3 = 2M\Omega$ , leading to a division factor of 10. The voltage drop at resistor  $R_3$  is then supplied to the Teensy's ADCs via a voltage follower.

### 3.2.2 Firmware

Like the firmware for the first version of Ekho, the advanced version is based on a design provided by Josiah Hester, Timothy Scott, and Jacob Sorber from Clemson University. For this thesis, the firmware was adopted for long-term deployment of Ekho in order to record harvesting environments without relying on external peripherals. Similar to the first version of Ekho, support for writing to the Teensy's SD Card and creating timestamps was added. Furthermore, the firmware is now capable of producing readable datasets in form of CSV files written to an SD Card, while the version from Clemson University recorded just raw bit fields.

#### Structure

Like the firmware of the first version, the program is divided into a `setup()` and a `loop()` function. The `setup` function is called just once after a reset, while the `loop()` function is called over and over again. In the `setup` function, the pins used to control the multiplexer and the transistor are configured as outputs. In addition, the Teensy's internal ADCs and the SD Card library are initialized and configured like explained in 3.1.2. The `loop()` function, which is continuously called by the main function, is provided by the Arduino core library. Each loop creates one I-V curve that consists of 64 I-V pairs. The resistance sweep differs from the first version since the transistor load, and the resistor multiplexer need to be controlled separately. The 64 I-V pairs are recorded with four different load resistors selected. Depending on the device under test, the number of measurements per selected load resistor is adjusted empirically to cover most of the I-V curve. The transistor load is used to create a finer detailed total load resistance for each selected load resistor. The transistors gate-source voltage  $V_{GS}$  is adjusted via the output of the Teensy's DAC.

# 4 Toolkit

In order to make the recorded datasets usable for experiments with energy harvesting wireless sensor nodes, a software toolkit has been created for this thesis. It is capable of maintaining an SQLite database that can hold multiple recorded harvesting environments and allows to perform repeatable and reproducible experiments in the area of energy harvesting and transient computing. Furthermore, a variety of simulation and visualization capabilities are already implemented in the toolkit and can easily be accessed via a simple Graphical User Interface (GUI).

The first part of the toolkit is a python script that automatically parses the recorded datasets from the CSV file into the SQLite database, shown in 4.1. Once the data has been inserted, it can be accessed via the GUI of the Surface profiler, like shown in figure 4.2 and further explained in section 4.2. In terms of visualisation, functionality to plot 2D I-V curves and MPP traces, as well as 3D I-V surfaces, is provided. Additionally, it is possible to simulate the charge of a buffer capacitor using a charging circuit similar to the one described in section 2.1.2. The user can specify various parameters that define the electrical and temporal characteristics of the load and the capacitor. Hence, it is possible to estimate what type of load can effectively be powered with a given harvester in a given recorded harvesting environment.

## 4.1 SQLite Database

The database consists of two tables: the measurement, and the datapoint table. The measurement table holds the name of the measurement (*measurement\_name*), the name of the profiled harvester (*device\_name*), and the time the recording has been initiated (*recording\_time*). Via a one-to-many relationship, multiple datapoints are referenced by a single measurement entity. The datapoint table holds single I-V pairs together with additional metadata, like the associated curve number (*curveNo*) and the time stamp (*time\_stamp*). Figure 4.1 shows the entity-relationship diagram of the SQLite database.

A small python script does the insertion of the recorded data into the database. The user enters the name of the measurement and the profiled device. Furthermore, the time and date when the measurement has been

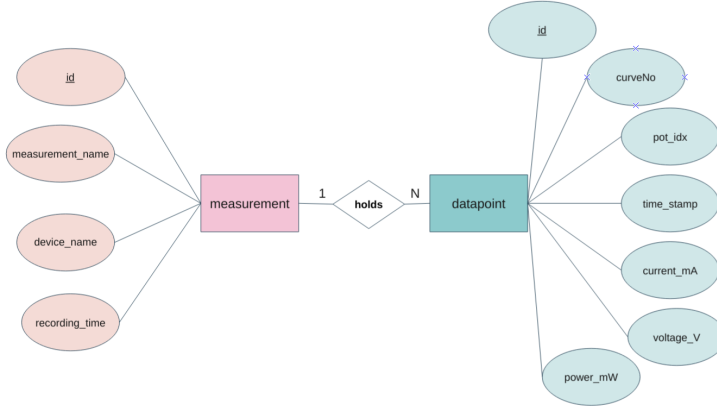


Figure 4.1: I-V database ER diagram

started must be entered manually since the Teensy's real-time clock resets upon every restart. With the entered start time and the timestamps recorded by the Teensy, the actual time each I-V curve has been recorded is recalculated. For filling the database, the SQL `INSERT INTO` statement is used. SQL queries are performed within the python program via the `sqlite3` module, which is a DB-API 2.0 interface for SQLite databases.

## 4.2 Surface profiler

The surface profiler, a python program with a graphical user interface, interacts with the SQLite database and features different types of visualisations and simulations based on the recorded data. The GUI is based on the *Tk* GUI toolkit, which is interfaced via the *Tkinter* python package. The user interface is composed of multiple *Tk* frames, which are displayed according to user input. For selecting a specific series of measurements, the first frame provides a dropdown combobox. After selecting a series of measurements, a database query is performed to fetch that specific measurement series's start- and end times. In the next frame, shown in figure 4.2, the user can further narrow that time range for further computations. In addition, the user must select whether the profiled harvester was a thermo-element or a solar panel. This selection is necessary to determine which model to use for curve fitting algorithms. Furthermore, the user may specify a sample rate division factor using a slider bar. Reducing the sampling rate reduces the number of datapoints used for further computations by the selected factor, reducing the computational effort. Afterwards, the user can select one of the visualization and simulation options described below.

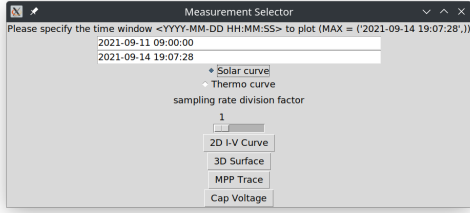


Figure 4.2: GUI to specify timeframe, sample rate, curve type, and processing option

### 4.2.1 2D I-V curve plots

The first visualisation option involves plotting I-V curves. Within the specified timeframe, all available I-V curves are plotted one after another. First, all I-V pairs from the selected measurement series within the specified time frame are fetched from the database. For each I-V curve, 64 data points are grouped and a curve-fitting algorithm is applied to the separate I-V pairs. The *curve\_fit* library function from the *scipy* module is used for curve fitting. It implements a non-linear least-squares analysis to fit a set of datapoints to a given reference function, determining n unknown function parameters. For harvesters based on the photovoltaic effect, equation 4.1, derived from equation 2.2, is used as the reference function supplied to the least squares analysis. For thermoelectric elements, the linear equation 4.2, derived from the equations 2.4 and 2.4 is used.

$$f(x) = a - c \cdot e^{b \cdot (x-d)} \quad (4.1)$$

$$f(x) = a * x + d \quad (4.2)$$

Once the parameters are obtained, the I-V curves are plotted using the *matplotlib* library. An example of an I-V curve derived from datapoints recorded by Ekho and plotted by this program is shown in figure 4.3.

### 4.2.2 3D I-V surface plots

In order to illustrate the temporal characteristics of a harvesting environment together with the I-V characteristics, support for 3D plots is implemented. The 3D surface plots feature an additional axis determined by the time an I-V curve has been recorded. The I-V curve is fetched similar to 2D plots via a curve fitting algorithm applied to the raw recorded I-V pairs. In each 3D plot, the x-axis corresponds to the measured voltage, the y-axis to the timestamp and the z-axis to the measured current. Tri-Surface plots from the *matplotlib* library are used to display the I-V surface. A Tri-Surface plot is created by triangulating a surface, such that every point on the surface

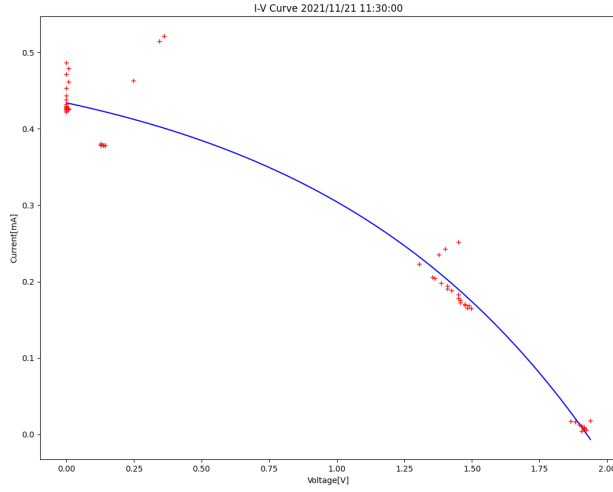


Figure 4.3: Solar I-V curve derived from datapoints recorded by Ekho

is a triangle. Consequently, the more I-V curves are supplied, the smoother the I-V surface will become. In figure 4.4 an exemplary I-V surface is shown that has been recorded over a period of four days.

#### 4.2.3 Maximum power point trace

In addition to the I-V plots, it is also possible to plot the Maximum Power Point (MPP) trace of a series of measurements. The MPP is the point in an I-V curve, where the power, the product of voltage  $V$  and current  $I$  is at a maximum. In order to obtain the MPP trace, the power is computed for each I-V pair within one time instant (i.e., one I-V curve). The maximum

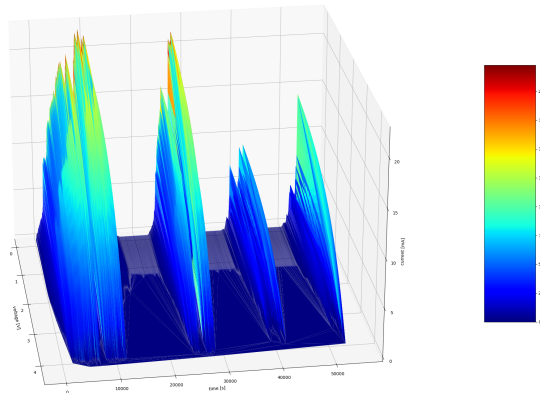


Figure 4.4: Solar I-V surface derived from datapoints recorded by Ekho

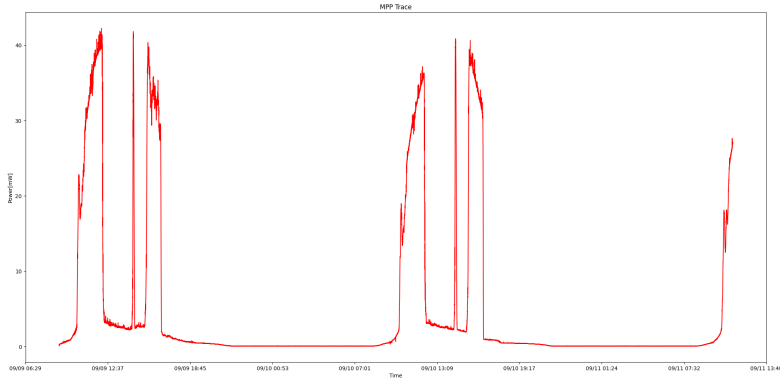


Figure 4.5: Solar I-V surface derived from datapoints recorded by Ekho

power of each curve is then plotted and provides a quick overview of the available harvested energy within a certain timeframe. Figure 4.5 shows an MPP trace of a harvester utilizing the photovoltaic effect. The MPP trace can provide a quick overview of the available harvested energy within a certain timeframe.

#### 4.2.4 Capacitor-charge model

In order to make the recorded datasets more accessible for researchers in the field of transient computing, a capacitor charge model has been implemented. The model is based on a simple harvesting circuit, like the one shown in figure 2.6. The capacitor voltage is computed over time for different behaviors of a load device. Again, the user can specify several parameters used the GUI, including the capacity of the used buffer capacitor, the current drain when the load is active and in sleep mode, and the threshhold voltages that determine when the load is active and when in sleep mode. Additionally, the discretisation rate, which determines the granularity of the discrete-time approximation used for modeling the capacitor charge, can be set.

##### Capacitor charge/discharge approximation

To calculate the capacitor voltage's transient behavior, the given time frame is discretised into  $k$  time fragments of length  $\tau$ . For each point in time, the capacitor voltage may be calculated by the time-continuous equation 4.3. By applying forward-Euler approximation, a discrete-time approximation can be derived from the time-continuous equation, as shown in equation 4.4.

$$V_C(t) = \frac{1}{C} \int I_H(t) - I_L(t) dt \quad (4.3)$$

$$\begin{aligned}
 V_{C(k)} &= V_{C(0)} + \frac{1}{C} \int_0^{(k-1)\tau} I_{H(t)} - I_L dt + \frac{1}{C} \int_{(k-1)\tau}^{k\tau} I_{H(t)} - I_L dt \\
 &= V_{C((k-1))} + \frac{1}{C} \int_{(k-1)\tau}^{k\tau} I_{H(t)} - I_L dt \quad (4.4) \\
 &\approx V_{C((k-1))} + \frac{1}{C} (I_{H(k-1)} - I_L) \tau
 \end{aligned}$$

$V_{C(k)}$  is the most recent computed capacitor voltage and  $\tau$  the size of each time fragment. Within one time fragment, the current supplied by the harvester  $I_{H(k)}$ , and the current drawn by the load  $I_L$  are assumed to remain constant. The current supplied by the harvester is obtained by evaluating the current I-V curve function calculated by the curve fitting algorithm, at  $V_{H(k-1)}$ . According to Kirchhoff's current law, the difference between the load's recent draw  $I_L$  and the current supplied by the harvester  $I_H$  forms the current charging or discharging the capacitor. Hence, an approximation of the new capacitor voltage  $V_{C(k)}$  can be calculated.

### Mode1: 'Greedy'

In the first mode, the capacitor is charged until an upper threshold ( $V_{up}$ ) is reached while the load remains in sleep mode. Once the upper threshold is surpassed, the load switches in active mode and draws more current. If the load's current draw is higher than the current supplied by the harvester, the capacitor will discharge until a lower threshold ( $V_{low}$ ) is reached. The lower threshold is the voltage, where the load can no longer work in active mode. If this model is compared to the Mementos approach described in 2.2, dropping below the upper threshold voltage  $V_{up}$  resembles the threshold voltage, where the load MCU starts to save the current execution state to non-volatile memory. The capacitor voltage and the current operating mode of the load is then plotted over time.

### Mode2: 'Periodic'

The second mode simulates a load that periodically switches from active to low-power mode. The program determines the number of active periods that pass without a power failure within a given time frame, and visualizes them together with the current capacitor voltage. The output of a 'Periodic' simulation is shown in figure 4.6.

## 4 Toolkit

---

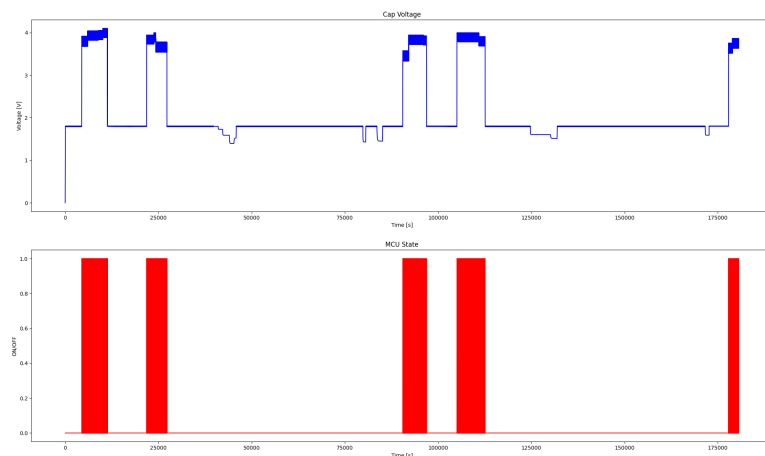


Figure 4.6: Mode2: 'Periodic' - on/off trace and capacitor voltage

# 5 Profiling Energy Harvesters

## 5.1 Harvested energy per harvester

The amount of harvested energy within a given time frame depends on the harvesting environment and the harvester under test. Therefore, multiple series of measurements have been recorded for each harvester to get a realistic picture of how powerful certain harvesters are and how they perform in different environmental conditions.

### 5.1.1 Solar Panels

Two different solar panels with an operating voltage of 3V have been profiled for this thesis: the more powerful but larger *PowerFilm SP3-37* and the smaller and less powerful *Panasonic AM-5610*.

#### PowerFilm SP3-37

The *PowerFilm SP3-37* is a  $21.17\text{cm}^2$  sized amorphous thin-film solar panel. The manufacturer claims a maximum power output of  $66\text{mW}$  when operated with an incoming solar power of  $1000\text{mW/m}^2$  (direct sun). During our experiments we observed a maximum power output of  $45.56\text{mW}$ , which is within the same order of magnitude. The electrical specifications claimed by the manufacturer, as well as the properties recorded by Ekho RevB, are shown in table 5.1 (“Datasheet SP3-37,” 2021).

|                                | <b>datasheet</b> | <b>measured</b>  |
|--------------------------------|------------------|------------------|
| <b>Power (full sun)</b>        | $66\text{mW}$    | $45.56\text{mW}$ |
| <b>Current @MPP (full sun)</b> | $22\text{mA}$    | $18.7\text{mA}$  |
| <b>Voltage @MPP (full sun)</b> | $3\text{V}$      | $2.43\text{V}$   |
| $V_{oc}$ (full sun)            | $4.6\text{V}$    | $4.36\text{V}$   |
| $I_{sc}$ (full sun)            | $28\text{mA}$    | $20.30\text{mA}$ |

Table 5.1: PowerFilm SP3-37: theoretical and measured electrical specifications

### Panasonic AM-5610

Similar to the PowerFilm panel, the *Panasonic AM-5610* solar panel is made out of amorphous silicon. However, with  $5\text{cm}^2$ , it is just one-quarter in size. A maximum power output of  $18\text{mW}$  at  $3.9\text{V}$  in direct sunlight ( $1000\text{mW/m}^2$ ) is specified by the manufacturer (“Amorphous Silicon Solar Cells,” 2019). The highest measured power output was  $17.04\text{mW}$ , which is close to the specified magnitude. Table 5.2 shows the specifications claimed by the manufacturer in comparison to the measured properties.

|                                | <b>datasheet</b> | <b>measured</b>  |
|--------------------------------|------------------|------------------|
| <b>Power (full sun)</b>        | $18\text{mW}$    | $17.04\text{mW}$ |
| <b>Current @MPP (full sun)</b> | $4.6\text{mA}$   | $3.93\text{mA}$  |
| <b>Voltage @MPP (full sun)</b> | $3.9\text{V}$    | $4.33\text{V}$   |
| $V_{oc}$ (full sun)            | $N/A$            | $5.4\text{V}$    |
| $I_{sc}$ (full sun)            | $N/A$            | $5.01\text{mA}$  |

Table 5.2: Panasonic AM-5610: theoretical and measured electrical specifications

#### 5.1.2 Impact of Shadowing, Weather and Season

The Experiments have shown, that shadowing, weather conditions and the current season have an significant impact on the delivered power of a specific solar panel.

On clear days in September, under direct solar radiation, the harvested power usually reaches  $40\text{mW}$ . However, when a shadow covers the harvester from direct sunlight, the harvested power decreases to just 10% ( $3 - 5\text{mW}$  for the *PowerFilmSP3 – 37*) of its original magnitude. Assuming an infinitely large energy storage, and an operation at the maximum power point, the electrical energy harvested  $W[\text{J}] = P_{mpp} \cdot \Delta t$  within a given period  $\Delta t$  can be determined. Figure 5.2 shows the harvested energy per hour on a clear day in September. The drop around 2 p.m. is the result of a passing shadow.

When operated on cloudy and rainy days in September, the power delivered by the *PowerFilmSP3 – 37* decreases from  $40\text{mW}$  to a magnitude of just ( $3 - 8\text{mW}$ ). In Figure 5.1 a comparison of the daily harvested energy on cloudy and clear days is presented.

Furthermore the impact of seasonal effects on the harvested energy like the angle of incidence of the sun’s radiation, as well as the daylight hours where observed. For this thesis, various experiments have been realised between between September and January. Figure 5.3 shows the hourly harvested energy by a *PowerFilmSP3 – 37* on a clear day in September and on a clear day in January. It can be observed, that there are seven

## 5 Profiling Energy Harvesters

---

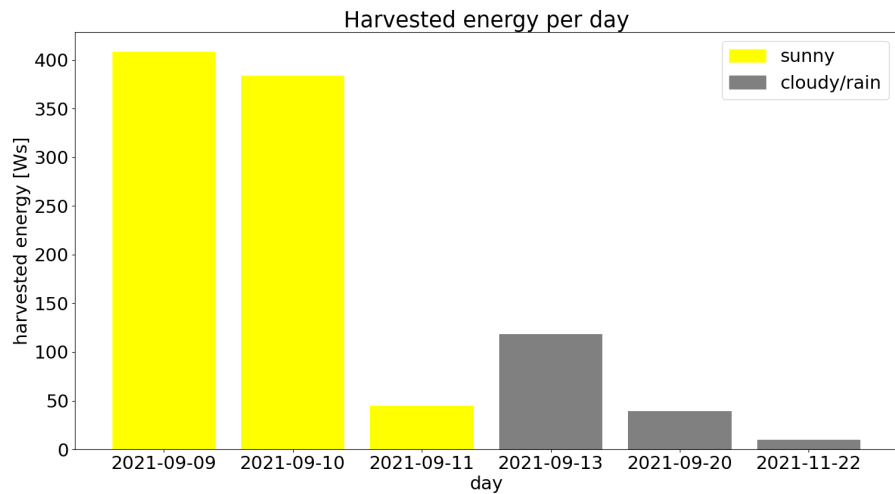


Figure 5.1: Energy harvested by a *PowerFilm SP3-37* solar panel on cloudy and sunny day

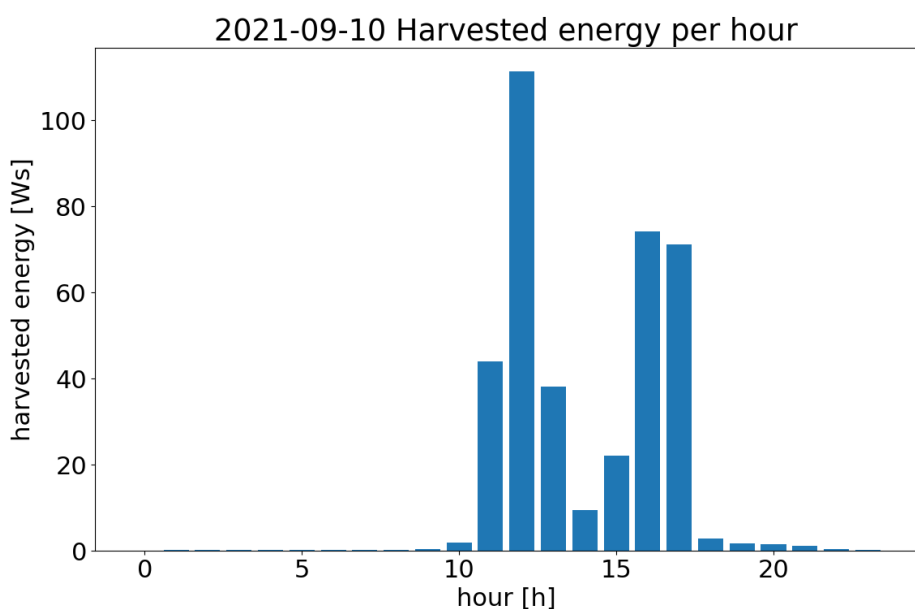


Figure 5.2: Hourly harvested energy by a *PowerFilm SP3-37* solar panel

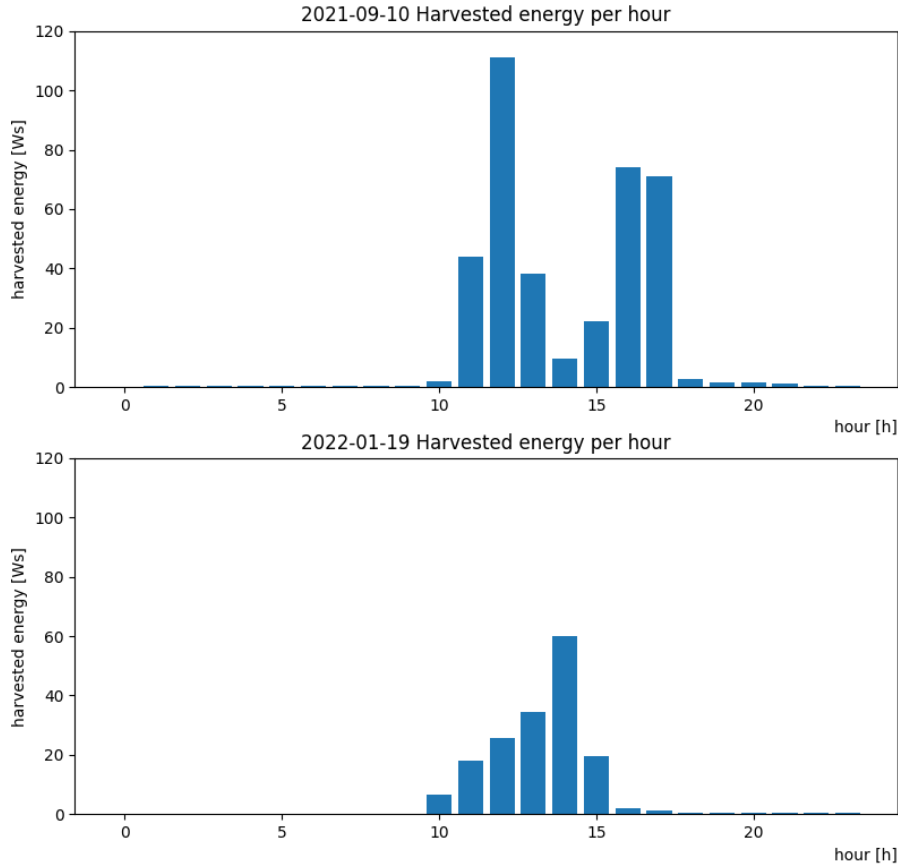


Figure 5.3: Harvested energy by a *PowerFilm SP3-37* on a clear day in September and on a clear day in January

hours with direct sunlight in September, while there are just five hours with sunlight in January at the place where the experiments have been performed. Additionally, the maximum harvested energy per hour reaches  $111.3\text{J}$  in September while in January it is never higher than  $59.89\text{J}$ . Together this leads to a decrease by 55.83% in daily harvested energy from  $383.79\text{J}$  down to  $169.51\text{J}$ .

### 5.1.3 Impact of the used solar panel

To compare the impact of the used solar panels, experiments have been carried out, where the *PowerFilmSP3 – 37* and the *PanasonicAM – 5610* were placed next to each other and profiled simultaneously. Table 5.3 shows the daily harvested energy and the harvested energy normalized to the

size of the used solar panel. It can be observed that the harvested energy in the same environment, within the same day, is between 29.4% to 42% lower for the Panasonic solar panel compared to the bigger PowerFilm panel. However, harvested energy per  $\text{cm}^2$  is between 1.878 and 3 times higher for the *Panasonic AM – 5610* panel.

| date       | device            | harvested energy | relative harvested energy |
|------------|-------------------|------------------|---------------------------|
| 2021-09-20 | PowerFilm SP3-37  | 39.34J           | 1.86J/ $\text{cm}^2$      |
| 2021-09-20 | Panasonic AM-5610 | 27.79J           | 5.56J/ $\text{cm}^2$      |
| 2021-09-21 | PowerFilm SP3-37  | 101.06J          | 4.77J/ $\text{cm}^2$      |
| 2021-09-21 | Panasonic AM-5610 | 58.29J           | 11.66J/ $\text{cm}^2$     |
| 2021-09-26 | PowerFilm SP3-37  | 325.11J          | 15.36J/ $\text{cm}^2$     |
| 2021-09-26 | Panasonic AM-5610 | 144.29J          | 28.86J/ $\text{cm}^2$     |

Table 5.3: Impact of the used solar panel

### 5.1.4 Thermoelectric Elements

In addition to the solar panels, a TEG (thermoelectric generator), the *Wakefield-Vette TEC-40-39-127* has been profiled. Since the *TEC-40-39-127* is marketed as a thermoelectric cooler rather than a thermoelectric generator, there is no reference data on the delivered power for a given applied temperature gradient. Therefore, a series of experiments have been set up.

**Radiator.** The first experiment involved placing the TEG on a radiator. The power output measured is depicted in figure 5.4. In order to keep the room temperature on a constant level, the radiator power level switched multiple times during a series of measurements, causing the peaks and lowerings in the MPP trace. The delivered power in this experiment maxed at  $0.03\text{mW}$  and  $60\text{mV}$ , while the maximum daily harvested energy reached  $0.11\text{J}$ . That is several orders of magnitude lower than the delivered power and the harvested energy by the tested solar panels.

**Masonry heater.** A similar experiment has been realized by placing the TEG on a masonry heater. The maximum delivered power in this setup reached  $0.1\text{mW}$ , while the harvested energy within a day reached  $4.35\text{J}$ .

**Hotplate.** As explained in 2.1.1, the harvested power directly corresponds to the applied temperature gradient. Since the harvested energy in the first experiments was very low, the following setup involved placing the TEG on a hotplate to achieve a greater temperature difference between the hot and cold sides. It shows that the power delivered significantly increases, reaching a maximum of  $17.66\text{mW}$  at  $2.15\text{V}$ , which is within the same order of magnitude as the power delivered by the profiled solar panels.

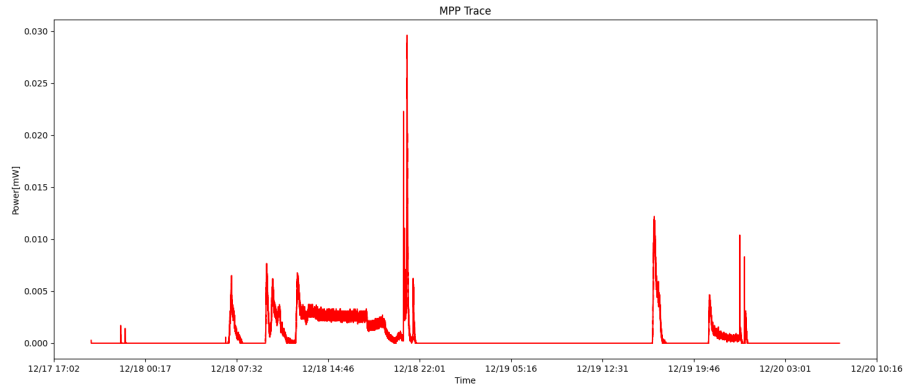


Figure 5.4: MPP trace of a Wakefield-Vette TEC-40-39-127 placed on a radiator

Additionally, attempts have been made to measure the amount of energy that can be harvested outdoors caused by differences in soil and air temperature. However, the energy harvested in such setups was too low to distinguish between delivered power and measurement noise.

In table 5.4, the results of the TEG measurements are summarized.

| Date       | Setup          | Harvested energy | Maximum power |
|------------|----------------|------------------|---------------|
| 2021-12-18 | radiator       | 0.11J            | 0.03mW        |
| 2021-12-26 | masonry heater | 4.35J            | 0.1mW         |
| 2021-12-25 | hotplate       | N/A              | 17.66mW       |

Table 5.4: Wakefield-Vette TEC-40-39-127: list of experiments

## 5.2 Greedy vs. periodic load behaviour

In section 5.1 the energy buffer is assumed infinitely big, and the harvester is assumed to operate in the maximum power point all the time. However, in scenarios considered for this thesis, the energy buffer will be just a small capacitor, and the operating point is varying as the capacitor charges and discharges. Hence, depending on the load's hardware and runtime behavior, just a proportion of the energy that can be harvested under ideal conditions will be gathered. To demonstrate this behaviour, we run a simulation for two different load scenario (i.e. 'greedy' and 'periodic') as described in section 4.2.4.

The simulation parameters need to be defined to estimate the harvested energy in the two modes. The simulated current draw is composed of the typical current draw of an *MSP430F* in active mode ( $4.32mA@16MHz/2.2V$ ),

and the current draw of a transmitting CC2420 ZigBee transceiver ( $11mA@P_{Tx} = -10dbm$ ) ("MSP430F22x2, MSP430F22x4 Mixed Signal Microcontroller datasheet (Rev. G)," 2021), ("CC2420," 2021). The capacitor size is set to  $0.01F$ . The MSP430 can operate with supply voltages between  $1.8V$  to  $3.6V$ , while the CC2420 is operational between  $2.1V$  and  $3.6V$ . Hence, the general threshold voltage in periodic and the upper threshold voltage in greedy mode are set to  $2.1V$ . The lower threshold voltage in greedy mode is set to  $1.8V$ , since only the MSP430 MCU needs to be active while saving the current execution state, as explained in 4.2.4. For the periodic mode, the on- ( $T_{on} = 50ms$ ) and off-time ( $T_{off} = 200ms$ ), as well as the current draw ( $I_{off} = 0.041mA$ ) by the MCU in LPMo mode are set. Table 5.5 shows a comparison of the maximum harvestable energy and the actually harvested energy in the periodic and greedy mode for some selected measurement series. Thermoelectric harvesters are not represented in the table because they don't reach the minimum voltage required for operating the simulated load.

| Date       | harvester         | MPP     | periodic | greedy  |
|------------|-------------------|---------|----------|---------|
| 2021-09-09 | PowerFilm SP3-37  | 408.20J | 172.61J  | 354.83J |
| 2021-09-10 | PowerFilm SP3-37  | 383.79J | 178.89J  | 397.80J |
| 2021-09-11 | PowerFilm SP3-37  | 626.87J | 235.74J  | 553.86J |
| 2021-09-26 | Panasonic AM-5610 | 144.29J | 88.08J   | 95.48J  |

Table 5.5: Harvested energy depending on load behaviour

It can be observed that with the given simulation input, the harvested energy in periodic mode reaches 42 to 61 percent of the available energy. In comparison, in greedy mode, 66 to 89 percent are reached.

### 5.3 Energy Harvesters as power supply

Using the recorded datasets, and the toolkit, it can be estimated which harvester in which harvesting environments can power the simulated load (*MSP430F+CC2420*). The first observations can be made by comparing the daily harvested energy with the energy that would be needed to power a load with a certain runtime behavior. The *MSP430F* MCU is assumed to operate in low-power (LPMo) mode for the period  $T_{off}$ , and then be active for  $T_{on}$  to read sensor data and transmit the collected data. The daily energy needed can then be calculated via equation 5.1, where  $DC$  is the duty cycle defined by  $T_{off}$  and  $T_{on}$ ,  $P_{active}$  and  $P_{LPM0}$ , the power consumption of the load in active- and low-power mode, and  $t_{day}$ , the number of seconds withining 24 hours.

$$E_{consumed}[J] = (DC \cdot P_{active} + (1 - DC) \cdot P_{LPM0}) \cdot t_{day} \quad (5.1)$$

Table 5.6 shows the required energy for various duty cycles.

| Duty Cycle | $T_{on}$ | $T_{off}$ | energy consumption |
|------------|----------|-----------|--------------------|
| 0.0014%    | 0.050s   | 3599.95s  | 7.83J              |
| 0.0083%    | 0.050s   | 599.95s   | 8.04J              |
| 0.0167%    | 0.050s   | 299.95s   | 8.28J              |
| 0.0833%    | 0.050s   | 59.95s    | 10.21J             |
| 0.5000%    | 0.050s   | 9.95s     | 22.31J             |
| 1.0000%    | 0.050s   | 4.95s     | 36.84J             |
| 4.7619%    | 0.050s   | 1.0s      | 146.09J            |

Table 5.6: Daily energy consumption for different duty cycles

The biggest solar panel, the *PowerFilm SP3-37* can deliver enough energy for all listed duty cycles when the harvesting environment is advantageous. Even on cloudy or rainy days, where solar radiation is low, the panel can still harvest enough daily energy for lower duty cycles up to 1%. The less powerful *Panasonic AM-5610*, can barely handle the 4.7619% duty cycle under ideal harvesting conditions. On days with low solar radiation, the harvested energy is sufficient for duty cycles up to 0.5%. The thermoelectric generator (*Wakefield-Vette TEC-40-39-127*), does only yield measurable results when the applied temperature gradient is high. Even on a masonry heater, the daily harvested energy is insufficient for very low duty cycles since the current draw of the load in low-power mode already exceeds the current delivered by the harvester.

Even though these first observations look promising, it has to be noted that they depict a very optimistic view. The daily harvested energy only applies when an operation of the harvester in the maximum power point and an infinitely large capacitor are assumed. In a system with just a tiny capacitor used as an energy buffer, the load will only operate during certain periods of a day when the currently delivered power is sufficient. In addition, the minimum voltage required for using the load has been ignored.

The actual periods in which enough energy is harvested to operate the load can be determined by the capacitor-charge model explained in 4.2.4. The parameters used for the simulation are the same as in section 5.2. Table 5.7 shows the total daily uptime in periodic and greedy mode. It can be observed that even for the *PowerFilm SP3-37* a good harvesting environment with high solar radiation (clear sky, no shadows) is needed to achieve a significant uptime. The smaller *Panasonic AM-5610* is not able to power the

## 5 Profiling Energy Harvesters

---

| Date       | Condition      | Harvester            | uptime periodic | uptime greedy |
|------------|----------------|----------------------|-----------------|---------------|
| 2021-09-09 | clear          | PowerFilm SP3-37     | 0 : 25 : 23     | 0 : 53 : 18   |
| 2021-09-10 | clear          | PowerFilm SP3-37     | 0 : 27 : 23     | 1 : 55 : 37   |
| 2021-09-11 | clear          | PowerFilm SP3-37     | 0 : 54 : 13     | 1 : 20 : 46   |
| 2021-09-21 | clear          | PowerFilm SP3-37     | 0 : 00 : 00     | 0 : 00 : 08   |
| 2021-12-23 | overcast       | PowerFilm SP3-37     | 0 : 00 : 00     | 0 : 00 : 0    |
| 2021-09-20 | overcast       | Panasonic AM-5610    | 0 : 00 : 00     | 0 : 00 : 0    |
| 2021-10-04 | clear          | Panasonic AM-5610    | 0 : 00 : 00     | 0 : 00 : 0    |
| 2021-10-04 | clear          | 2x Panasonic AM-5610 | 0 : 00 : 00     | 0 : 00 : 00   |
| 2021-10-04 | clear          | 4x Panasonic AM-5610 | 0 : 28 : 19     | 0 : 47 : 04   |
| 2021-12-25 | hotplate       | TEC-40-39-127        | 0 : 0 : 10*     | 0 : 00 : 00*  |
| 2021-12-26 | masonry heater | TEC-40-39-127        | 0 : 00 : 00     | 0 : 00 : 00   |
| 2021-12-18 | radiator       | TEC-40-39-127        | 0 : 00 : 00     | 0 : 00 : 00   |

Table 5.7: Simulated on-time in periodic and greedy mode:  $T_{on} = 250ms$ (periodic),  $T_{off} = 50ms$ (periodic),  $C = 0.01F$ ,  $I_{on} = 15.32mA$ ,  $I_{off} = 0.041$ (periodic),  $I_{off} = 0mA$ (greedy),  $V_{up} = 2.1V$ ,  $V_{low} = 1.8V$   
\*total experiment duration 0 : 01 : 14

simulated load in any of the recorded harvesting environments. However, a parallel circuit of four panels (4x *Panasonic AM-5610*) operated on a sunny day, yields an uptime of 0:28:19 in periodic, and 0:47:04 in greedy mode. The thermoelectric element can only drive the load in environments with extreme temperature gradients, like in the experiment where the element has been placed on a hotplate. In less extreme environments with applied temperature differences between 10 °C and 20 °C, like on a masonry heater, the largest achieved voltage is still below the threshold required to operate the load directly without additional converter circuits. One reason why periodic load behaviour is worse than greedy in terms of uptime is that in periodic mode the load still draws a low current while in sleep mode.

# 6 Evaluation

In this chapter, the two revisions of Ekho are evaluated in terms of measurement accuracy.

## Teensy 3.6

The Teensy 3.6 development board receives analog signals from the Ekho board and uses its internal ADCs to convert them into digital values. The resolution of the Teensy's internal ADCs has been set to 12 bits for all experiments carried out for this thesis. With a full-scale range of  $V_{FSR} = V_{REF} = 3.3V$ , the voltage corresponding to the least significant bit  $V_{LSB}$  equals  $0.81mV$ . Since there is no further information on the accuracy of the ADC available in the datasheet of the MCU ("Kinetis K66 Sub-Family," 2017), the conversion error has been determined by a series of measurements. As shown in table 6.1, the relative measurement error is high (up to 83%) in the lower-end of the ADC's conversion range. However, accuracy is sufficient in most of the conversion range, with a relative conversion error between 1.17% and 2.00%.

## Ekho RevA

In addition to the measurement error caused by the Teensy's ADCs, the analog frontend adds further measurement uncertainties. The voltage sense implementation holds known systematic measurement deviations that are caused by the simplification  $R_5 \ll (R_{load} \parallel (R_2 + R_3))$  and  $R_{load} \ll (R_2 + R_3)$ , as described in section 3.1.1. Furthermore, the limited precision of the used resistors and the programmable gain amplifiers are a cause of measurement deviations. The total relative measurement error of the whole Ekho RevA system for various harvester currents and voltages is depicted in table 6.2. It shows that the voltage sense measurement error stays between 6.25% and 7.00% through the whole operating range. The current sense measurement error decreases from 53.08% down to 0.68%, when the harvester current increases.

## Ekho RevB

The second revision of the analog frontend brings other flaws that cause measurement deviations. As described in section 3.2.1, the current sense

## 6 Evaluation

---

| <b>applied voltage</b> | <b>ADC value</b> | <b>measured voltage</b> | <b><math>\Delta V</math></b> | <b>error rel.</b> |
|------------------------|------------------|-------------------------|------------------------------|-------------------|
| 0V                     | 0                | 0,0000V                 | 0,0000V                      | 0,00%             |
| 0,001V                 | 1                | 0,0008V                 | 0,0002V                      | 19,43%            |
| 0,002V                 | 1                | 0,0008V                 | 0,0012V                      | 59,72%            |
| 0,003V                 | 1                | 0,0008V                 | 0,0022V                      | 73,14%            |
| 0,005V                 | 1                | 0,0008V                 | 0,0042V                      | 83,89%            |
| 0,01V                  | 6                | 0,0048V                 | 0,0052V                      | 51,66%            |
| 0,02V                  | 19               | 0,0153V                 | 0,0047V                      | 23,46%            |
| 0,03V                  | 32               | 0,0258V                 | 0,0042V                      | 14,06%            |
| 0,04V                  | 42               | 0,0338V                 | 0,0062V                      | 15,41%            |
| 0,05V                  | 57               | 0,0459V                 | 0,0041V                      | 8,15%             |
| 0,1V                   | 117              | 0,0943V                 | 0,0057V                      | 5,74%             |
| 0,55V                  | 669              | 0,5390V                 | 0,0110V                      | 2,00%             |
| 1,1V                   | 1346             | 1,0844V                 | 0,0156V                      | 1,42%             |
| 1,65V                  | 2024             | 1,6307V                 | 0,0193V                      | 1,17%             |
| 2,2V                   | 2697             | 2,1729V                 | 0,0271V                      | 1,23%             |
| 2,75V                  | 3372             | 2,7167V                 | 0,0333V                      | 1,21%             |
| 3,3V                   | 4048             | 3,2613V                 | 0,0387V                      | 1,17%             |

Table 6.1: Teensy 3.6 ADC: conversion error

| <b>applied voltage</b> | <b>applied current</b> | <b>measured voltage</b> | <b>measured current</b> | <b>error rel. voltage</b> | <b>error rel. current</b> |
|------------------------|------------------------|-------------------------|-------------------------|---------------------------|---------------------------|
| 0V                     | 0mA                    | 0,0113V                 | -0,0564mA               | 0,00%                     | 0%                        |
| 0,275V                 | 0,3mA                  | 0,2578V                 | 0,4592mA                | 6,25%                     | 53,08%                    |
| 0,55V                  | 0,83mA                 | 0,5156V                 | 0,9587mA                | 6,25%                     | 15,51%                    |
| 0,825V                 | 1,36mA                 | 0,7686V                 | 1,4824mA                | 6,84%                     | 9,00%                     |
| 0,902V                 | 1,5mA                  | 0,8395V                 | 1,6234mA                | 6,93%                     | 8,23%                     |
| 1,3V                   | 2,26mA                 | 1,2101V                 | 2,3284mA                | 6,91%                     | 3,03%                     |
| 1,65V                  | 2,93mA                 | 1,5356V                 | 2,9850mA                | 6,93%                     | 1,88%                     |
| 1,89V                  | 3,39mA                 | 1,7596V                 | 3,4321mA                | 6,90%                     | 1,24%                     |
| 2,2V                   | 3,96mA                 | 2,0496V                 | 3,9921mA                | 6,84%                     | 0,81%                     |
| 2,475V                 | 4,46mA                 | 2,3058V                 | 4,4755mA                | 6,84%                     | 0,35%                     |
| 2,75V                  | 5,01mA                 | 2,5588V                 | 5,0153mA                | 6,95%                     | 0,10%                     |
| 3,025V                 | 5,55mA                 | 2,8134V                 | 5,5309mA                | 7,00%                     | 0,34%                     |
| 3,3V                   | 6,08mA                 | 3,0696V                 | 6,0385mA                | 6,98%                     | 0,68%                     |

Table 6.2: Total measurement error Ecko RevA

circuit is switched in parallel to the voltage sense circuit. Although the volt-

## 6 Evaluation

---

age sense paths resistance is much higher valued than the resistance of the current sense path, a minor current divider is always noticeable. That effect increases when higher-valued resistors are selected via the multiplexer. The voltage sense circuit contains a 1/10 voltage divider. This voltage division shrinks the input voltage of the Teensy to a lower level. For small measured voltages, the ADC then operates in a range with significant conversion error. Table 6.3 shows the experimentally determined measurement errors of the whole Ekho RevB system for different multiplexer resistors, harvester voltages, and harvester currents.

| applied voltage | applied current | measured voltage | measured current | error rel. voltage | error rel. current | DAC value | Resistor |
|-----------------|-----------------|------------------|------------------|--------------------|--------------------|-----------|----------|
| 0,274V          | 0,01mA          | 0,06V            | 0mA              | 78,10%             | 100,00%            | 606       | 100kΩ    |
| 1,6V            | 0,01mA          | 1,74V            | 0,01mA           | -8,75%             | 0,00%              | 1212      | 100kΩ    |
| 2,4V            | 0,01mA          | 2,53V            | 0mA              | -5,42%             | 100,00%            | 587       | 100kΩ    |
| 3,2V            | 0,01mA          | 3,33V            | 0,01mA           | -4,06%             | 0,00%              | 674       | 100kΩ    |
| 4V              | 0,01mA          | 4,11V            | 0,01mA           | -2,75%             | 0,00%              | 681       | 100kΩ    |
| 0,274V          | 0,06mA          | 0,04V            | 0,04mA           | 85,40%             | 33,33%             | 1065      | 5.1kΩ    |
| 1,6V            | 0,17mA          | 1,76V            | 0,17mA           | -10,00%            | 0,00%              | 1057      | 5.1kΩ    |
| 2,4V            | 0,17mA          | 2,54V            | 0,17mA           | -5,83%             | 0,00%              | 1069      | 5.1kΩ    |
| 3,2V            | 0,17mA          | 3,32V            | 0,17mA           | -3,75%             | 0,00%              | 1076      | 5.1kΩ    |
| 4V              | 0,17mA          | 4,11V            | 0,17mA           | -2,75%             | 0,00%              | 1088      | 5.1kΩ    |
| 0,274V          | 0,27mA          | 0,07V            | 0,26mA           | 74,45%             | 3,70%              | 802       | 1kΩ      |
| 1,6V            | 0,55mA          | 1,77V            | 0,55mA           | -10,63%            | 0,00%              | 696       | 1kΩ      |
| 2,4V            | 0,6mA           | 2,54V            | 0,59mA           | -5,83%             | 1,67%              | 741       | 1kΩ      |
| 3,2V            | 0,64mA          | 3,33V            | 0,63mA           | -4,06%             | 1,56%              | 793       | 1kΩ      |
| 4V              | 0,65mA          | 4,11V            | 0,64mA           | -2,75%             | 1,54%              | 796       | 1kΩ      |
| 0,274V          | 1,51mA          | 0,08V            | 1,55mA           | 70,80%             | -2,65%             | 100       | 51Ω      |
| 1,6V            | 3,03mA          | 1,67V            | 3,12mA           | -4,37%             | -2,97%             | 200       | 51Ω      |
| 2,4V            | 3,79mA          | 2,43V            | 3,91mA           | -1,25%             | -3,17%             | 250       | 51Ω      |
| 3,2V            | 4,56mA          | 3,22V            | 4,69mA           | -0,63%             | -2,85%             | 300       | 51Ω      |
| 4V              | 6,84mA          | 3,93V            | 7,04mA           | 1,75%              | -2,92%             | 450       | 51Ω      |

Table 6.3: Total measurement error Ekho RevB

It can be observed that for lower voltages, the Ekho RevA works better than the Ekho RevB, while the Ekho RevB is also capable of accurately measuring voltages above 3V.

## 7 Limitations

As described in section 6, measurement accuracy is limited, especially for very low voltages and currents. Hence, it isn't easy to profile harvesters in environments that don't provide a lot of harvestable energy. With the given Ekho designs, it was impossible to accurately profile thermoelectric harvesters in setups with low-temperature gradients.

Furthermore, the current implementation of the firmware significantly limits the number of samples that can be recorded per second. The performance is more than sufficient for profiling solar panels and thermoelectric generators but might be insufficient to profile harvesters with more volatile sources, like radiofrequency sources. Apart from accuracy and performance limits, it is challenging to depict weather conditions accurately. One can describe the weather conditions on a particular day as "clear", but the sky might still be covered with clouds for a short period of time that day. If a cloud covers the sun within the small time frame at noon, where most of the energy is harvested, the overall harvested energy will decrease significantly, even if the rest of the day is sunny.

Moreover, the capacitor-charge model does not include a voltage regulation stage. Hence, there are cases where the simulation outputs that the load cannot be operated in the given environment. However, an operation might be possible if a boost-converter is used. Additionally, the capacitor-charge simulation implemented in the toolkit can be quite time-consuming when a fine-grained temporal discretization is used.

## 8 Future Work

The measurement accuracy for low-energy harvesters like thermoelectric elements could be further increased by adjusting the voltage divider on the Ekho RevB to better fit the input range of the Teensy's ADC. The sample frequency could be raised by directly storing the read ADC values onto the SD Card instead of converting them into voltage and current values. The problem in describing weather conditions could be solved by operating a pyranometer next to the solar panel under test to directly record solar radiations to allow a more precise comparison of different solar panels. The capacitor-voltage simulation time can be further reduced by adjusting the program to support multi-threading. To complement the already implemented simulations, one could built an emulator that can replay the collected I-V surfaces. Additionally, further harvesters could be profiled over longer periods of time, to better cover seasonal dependencies.

## 9 Conclusion

In this thesis the applicability of using energy harvesters like solar panels or thermoelectric elements to power mobile devices within the internet of things has been evaluated. When novel solutions like transient computing are combined with energy harvesting, detailed profiles of harvesters in various harvesting environments are crucial for making experiments repeatable and enabling efficient debugging and verification.

Two different versions of the Ekho recorder have been rebuilt to profile various energy harvesters in different harvesting environments. They can emulate various load resistances and record currents and voltages in various operating points, forming I-V curves. A database has been implemented to make the recorded data accessible for researchers in the area of transient computing. A small python script is provided that enables an automated insertion of the recorded datasets.

To analyze recorded I-V surfaces, a software toolkit with a GUI, the Surface profiler, has been implemented. It features functionality to visualize the recorded data as 2D I-V curves, 3D I-V surfaces, MPP traces, and energy histograms. Additionally, the charge of a buffer capacitor in a simulated harvesting circuit can be determined, enabling estimations on which type of load can be powered with a given harvester in a given harvesting environment.

The Ekho recorders and the Surface profiler have been used to analyze two different solar panels and a thermoelectric harvester in various harvesting environments. In total, 48 days of harvesting activity have been recorded and made available via the database.

The recorded data showed that for both profiled solar panels, under all recorded environmental conditions, the total daily harvested energy is sufficient to power a simulated load consisting of an MCU (MSP430F) and a transmitting CC2420 ZigBee transceiver. However, the capacitor charge simulation shows, that with just a tiny energy buffer (0.01F) and without a boost converter, there are far less scenarios in which the load device could be operated. In fact, only the  $21,17\text{cm}^2$  sized *PowerFilm SP3-37* was able to power the specified load, and also only under direct sunlight.

Furthermore, the recordings show that thermoelectric elements like the *Wakefield-Vette TEC-40-39-127* are only able to power the simulated load when high-temperature differences are applied. Temperature gradients between soil and air, emerging from day/night cycles, are insufficient to power

## 9 Conclusion

---

the simulated load. Other experiments that involved placing the element on a masonry heater or a hotplate yielded enough energy to power the simulated load.

# Bibliography

- Ahmed, F., Ahmed, T., Muhammad, Y., Le Moullec, Y., & Annus, P. (2016). Operating wireless sensor nodes without energy storage: Experimental results with transient computing. *Electronics*, 5(4). <https://doi.org/10.3390/electronics5040089> (cit. on p. 12)
- Ahmed, F., Kervadec, C., Le Moullec, Y., Tamberg, G., & Annus, P. (2018a). Autonomous Wireless Sensor Networks: Implementation of Transient Computing and Energy Prediction for Improved Node Performance and Link Quality. *The Computer Journal*, 62(6), 820–837. <https://doi.org/10.1093/comjnl/bxy101> (cit. on p. 10)
- Ahmed, F., Kervadec, C., Le Moullec, Y., Tamberg, G., & Annus, P. (2018b). Autonomous Wireless Sensor Networks: Implementation of Transient Computing and Energy Prediction for Improved Node Performance and Link Quality. *The Computer Journal*, 62(6), 820–837. <https://doi.org/10.1093/comjnl/bxy101> (cit. on p. 13)
- Alternative energy in power electronics (First edition..). (2015). (Cit. on p. 8).
- Amorphous silicon solar cells. (2019). [https://mediap.industry.panasonic.eu/assets/download-files/import/ca\\_amorton\\_solar\\_cells\\_en.pdf](https://mediap.industry.panasonic.eu/assets/download-files/import/ca_amorton_solar_cells_en.pdf) (cit. on p. 35)
- Ap2112 datasheet. (2017). <https://www.diodes.com/assets/Datasheets/AP2112.pdf> (cit. on p. 18)
- Balsamo, D., Weddell, A. S., Merrett, G. V., Al-Hashimi, B. M., Brunelli, D., & Benini, L. (2015). Hibernus: Sustaining computation during intermittent supply for energy-harvesting systems. *IEEE Embedded Systems Letters*, 7(1), 15–18. <https://doi.org/10.1109/LES.2014.2371494> (cit. on p. 13)
- Cao, S., & Li, J. (2017). A survey on ambient energy sources and harvesting methods for structural health monitoring applications. *Advances in Mechanical Engineering*, 9(4), 1687814017696210. <https://doi.org/10.1177/1687814017696210> (cit. on p. 5)
- Cc2420. (2021). <https://www.ti.com/lit/ds/symlink/cc2420.pdf?ts=1640692667723> (cit. on p. 40)
- Chen, Y. (2019). Energy harvesting communications : : Principles and theories (1st edition.). (Cit. on p. 9).
- Datasheet ad5241/ad5242. (2015). <https://www.analog.com/media/en/technical-documentation/data-sheets/AD5241-5242.pdf> (cit. on p. 20)

## Bibliography

---

- Datasheet sp3-37. (2021). <https://www.powerfilmsolar.com/media/products/SP337-71AEA337D2954.pdf> (cit. on p. 34)
- Datasheet tmux1104. (2020). [https://www.ti.com/lit/ds/symlink/tmux1104.pdf?HQS=dis-mous-null-mousemode-dsf-pf-null-wwe&DCM=yes&ref\\_url=https%5C%3A%5C%2F%5C%2Fwww.mouser.at%5C%2F&distId=26#page=23&zoom=100,0,512](https://www.ti.com/lit/ds/symlink/tmux1104.pdf?HQS=dis-mous-null-mousemode-dsf-pf-null-wwe&DCM=yes&ref_url=https%5C%3A%5C%2F%5C%2Fwww.mouser.at%5C%2F&distId=26#page=23&zoom=100,0,512) (cit. on p. 24)
- Energy harvesting for autonomous systems*. (2010). (Cit. on pp. 4, 5, 8, 11).
- Hande, A., Polk, T., Walker, W., & Bhatia, D. (2007). Indoor solar energy harvesting for sensor network router nodes [Special Issue on Sensor Systems]. *Microprocessors and Microsystems*, 31(6), 420–432. <https://doi.org/https://doi.org/10.1016/j.micpro.2007.02.006> (cit. on p. 6)
- Hester, J., Scott, T., & Sorber, J. (2014). Ekho: Realistic and repeatable experimentation for tiny energy-harvesting sensors. *Sensys 2014 - Proceedings of the 12th ACM Conference on Embedded Networked Sensor Systems*. <https://doi.org/10.1145/2668332.2668336> (cit. on pp. 1, 2, 17)
- Ikeda, N., Shigeta, R., Shiomi, J., & Kawahara, Y. (2020). Soil-monitoring sensor powered by temperature difference between air and shallow underground soil. *Proc. ACM Interact. Mob. Wearable Ubiquitous Technol.*, 4(1). <https://doi.org/10.1145/3380995> (cit. on p. 14)
- Im, Kim, Lee, K., Woo, Eom, Choi, C.-S., & Moon, H. (2020). Self-powered autonomous wireless sensor node by using silicon-based 3d thermo-electric energy generator for environmental monitoring application. *Energies*, 13, 674. <https://doi.org/10.3390/en13030674> (cit. on p. 13)
- Josiah Hester, J. S., Timothy Scott. (2019). Ekho: Realistic and repeatable experimentation for tiny energy-harvesting sensors. (Cit. on p. 20).
- Jushi, A., Pegatoquet, A., & Le, T. N. (2016). Wind energy harvesting for autonomous wireless sensor networks. *2016 Euromicro Conference on Digital System Design (DSD)*, 301–308. <https://doi.org/10.1109/DSD.2016.43> (cit. on p. 1)
- Kinetis k66 sub-family. (2017). <https://www.nxp.com/docs/en/data-sheet/K66P144M180SF5V2.pdf> (cit. on pp. 17, 43)
- Li, Y., & Shi, R. (2015). An intelligent solar energy-harvesting system for wireless sensor networks. *EURASIP Journal on Wireless Communications and Networking*, 2015, 179. <https://doi.org/10.1186/s13638-015-0414-2> (cit. on p. 13)
- Lyden, S., & Ji, T. (2020). A study into the impact of the choice of maximum power point tracking technique on the reliability of the power electronics interface for photovoltaic systems. *2020 Australasian Universities Power Engineering Conference (AUPEC)*, 1–5 (cit. on p. 8).
- Max9939 datasheet. (2019). <https://datasheets.maximintegrated.com/en/ds/MAX9939.pdf> (cit. on p. 18)

## Bibliography

---

- Merrett, G. V. (2016). Invited: Energy harvesting and transient computing: A paradigm shift for embedded systems? *2016 53nd ACM/EDAC/IEEE Design Automation Conference (DAC)*, 1–2. <https://doi.org/10.1145/2897937.2905011> (cit. on p. 2)
- Msp430f22x2, msp430f22x4 mixed signal microcontroller datasheet (rev. g). (2021). <https://www.ti.com/lit/gpn/msp430f2274> (cit. on pp. 11, 40)
- Mustansar Hussain, C. (Ed.). (2018). Chapter 41 - engineered nanomaterials for energy applications. In *Handbook of nanomaterials for industrial applications* (pp. 751–767). Elsevier. <https://doi.org/10.1016/B978-0-12-813351-4.00043-2>. (Cit. on p. 8)
- Nesarajah, M., & Frey, G. (2016). Thermoelectric power generation: Peltier element versus thermoelectric generator. *IECON 2016 - 42nd Annual Conference of the IEEE Industrial Electronics Society*, 4252–4257. <https://doi.org/10.1109/IECON.2016.7793029> (cit. on p. 8)
- Oh, T., Islam, S. K., To, G., & Mahfouz, M. (2017). Powering wearable sensors with a low-power cmos piezoelectric energy harvesting circuit. *2017 IEEE International Symposium on Medical Measurements and Applications (MeMeA)*, 308–313. <https://doi.org/10.1109/MeMeA.2017.7985894> (cit. on p. 5)
- Panahi, F. H., Moshirvaziri, S., Mihemmedi, Y., Panahi, F. H., & Ohtsuki, T. (2018). Smart energy harvesting for internet of things. *2018 Smart Grid Conference (SGC)*, 1–5. <https://doi.org/10.1109/SGC.2018.8777889> (cit. on p. 1)
- Ransford, B., Sorber, J., & Fu, K. (2011). Mementos: System support for long-running computation on rfid-scale devices. *Sigplan Notices - SIGPLAN*, 47, 159–170. <https://doi.org/10.1145/2248487.1950386> (cit. on p. 13)
- Shaikh, F. K., & Zeadally, S. (2016). Energy harvesting in wireless sensor networks: A comprehensive review. *Renewable and Sustainable Energy Reviews*, 55, 1041–1054. <https://doi.org/10.1016/j.rser.2015.11.010> (cit. on p. 12)
- Teensy® 3.6 development board. (2017). <https://www.pjrc.com/store/teensy36.html> (cit. on p. 17)